



# Horizontal Force Required for Subduction Initiation at Passive Margins With Constraints From Slab Detachment

Lorenzo G. Candiotti<sup>1\*</sup>, Thibault Duretz<sup>2</sup> and Stefan M. Schmalholz<sup>1</sup>

<sup>1</sup>Institut des Sciences de la Terre, Université de Lausanne, Lausanne, Switzerland, <sup>2</sup>Institut für Geowissenschaften, Goethe-Universität Frankfurt, Frankfurt, Germany

## OPEN ACCESS

### Edited by:

Fabio Crameri,  
Undertone.design, Switzerland

### Reviewed by:

Elvira Mulyukova,  
Northwestern University,  
United States  
Carmen Gaina,  
Queensland University of Technology,  
Australia

### \*Correspondence:

Lorenzo G. Candiotti  
lorenzo.candiotti@unil.ch

### Specialty section:

This article was submitted to  
Structural Geology and Tectonics,  
a section of the journal  
Frontiers in Earth Science

**Received:** 29 September 2021

**Accepted:** 25 March 2022

**Published:** 04 May 2022

### Citation:

Candiotti LG, Duretz T and  
Schmalholz SM (2022) Horizontal  
Force Required for Subduction  
Initiation at Passive Margins With  
Constraints From Slab Detachment.  
Front. Earth Sci. 10:785418.  
doi: 10.3389/feart.2022.785418

Subduction zones are essential drivers of plate tectonics. However, the processes causing subduction zone initiation (SZI), involving the formation of a new plate boundary, and the forces required remain disputed. Here, we focus on horizontally forced SZI at passive margins and quantify the horizontal force required for SZI with two-dimensional petrological-thermomechanical numerical models. The initial configuration, involving two passive margins bounding a 400 km wide basin with exhumed mantle, is calculated by a numerical rifting simulation to guarantee thermomechanical feasibility and isostatic equilibrium. SZI occurs at one passive margin during convergence of the basin-margin system. SZI is caused by thermal softening due to local shear heating. A local temperature increase of only ca. 50°C is sufficient to cause SZI. Corresponding simulations without shear heating do not show SZI, showing unequivocally that thermal softening controls SZI. We systematically limit the lithospheric deviatoric stress to determine the minimum force required for SZI. A minimum force (per unit length) of ca. 14 TN m<sup>-1</sup> is required for SZI; a force magnitude that agrees with independent estimates from mantle convection models. However, for the associated stress limit of 200 MPa the lithosphere is so weak that slab detachment (SD) already occurs at the onset of basin closure in the horizontal, non-subducted region of the subducting plate. Only for stress limits > =300 MPa (yielding a force of ca. 15 TN m<sup>-1</sup>) subduction of continental crust occurs and SD occurs in the subducted slab. The force required for SZI is a proxy for the effective compressive lithospheric strength. This strength also controls subsequent SD due to tensile slab pull, which increases during subduction, also since our models include the olivine–wadsleyite phase change. Our simulations show a causal link between SZI and subsequent SD: If forces required for SZI are smaller, then the lithosphere is weaker and then SD occurs at shallower levels and corresponding slabs are shorter. Concerning the European Alps, our results imply that if there was no SD since the Europe–Adria collision some 30 Myr ago (as proposed by some studies), then the subducted lithosphere must be considerably strong.

**Keywords:** Convergent plate boundary formation, subduction zone initiation, thermal softening, shear heating, slab detachment, lithospheric strength, plate driving force, Alps

## 1 INTRODUCTION

Earth is the only planet in our Solar System known to have currently active plate tectonics. Subduction zones, where old lithosphere is recycled back into the mantle, are major drivers of plate motion. However, the mechanisms that form convergent plate boundaries and create new subduction zones remain elusive (Stern, 2004; Stern and Gerya, 2018; Cramer et al., 2020). Two conceptual endmember scenarios for subduction zone initiation (SZI) have been proposed in the past decades: spontaneous, or vertically-forced, and induced, or horizontally-forced SZI (Stern, 2004; Stern and Gerya, 2018; Cramer et al., 2020). Vertically-forced SZI is supposedly driven by the increasing density, and therefore buoyancy, contrast between cooling oceanic lithosphere moving away from mid-ocean ridges and the underlying mantle. The feasibility of this scenario is disputed (e.g., Mueller and Phillips, 1991), particularly for SZI at passive margins. Cloetingh et al. (1989) already estimated that if SZI is not successful by ca. 20 Myr after continental break-up, the body force arising from density contrasts is likely insufficient to break the oceanic lithosphere. In fact, old ages of ocean floor (e.g., Müller et al., 2008) and various data collected from recent and ancient subduction zones (Cramer et al., 2020; Lallemand and Arcay, 2021) indicate that vertically-forced SZI was unlikely the dominant scenario during the last ca. 100 Myr. Instead, an additional horizontal compressive force, i.e., horizontally-forced SZI (McKenzie, 1977; Cramer et al., 2020), is required to overcome the increasing strength of cooling oceanic lithosphere. Recent geophysical observations of the Puysegur plate boundary south of New Zealand suggest that horizontal forces initially dominate at the site of SZI, but with time, vertical forces can accelerate, propagate along strike and facilitate the development of self-sustaining subduction (Shuck et al., 2022). However, both the horizontal force required for SZI as well as the processes causing strain localization and creating a new plate boundary remain poorly constrained.

Due to the large time and spatial scales, the complex petrological-thermomechanical feedbacks and the sparsity of geological evidence for SZI on present-day Earth (e.g., Cramer et al., 2020), a suitable method to study SZI is numerical geodynamic modelling. Published numerical models of SZI can be classified in two categories: 1) Models that investigate SZI at already existing, weak plate boundaries, which are prescribed as weak zones in the initial model configuration. These studies focus on the onset of sinking of a lithospheric plate and sometimes on the subduction of one plate below another plate (e.g., Malatesta et al., 2013; Zhong and Li, 2020; Zhou et al., 2020; Zhou and Wada, 2021). These studies do not investigate the formation of a new convergent plate boundary associated with SZI. 2) Models that investigate both SZI and the associated formation of a new convergent plate boundary, without *a priori* prescribing an already existing weak plate boundary in the initial model configuration (e.g., Thielmann and Kaus, 2012; Auzemery et al., 2020; Kiss et al., 2020; Candiotti et al., 2021). The plate boundary formation must be numerically simulated in these models and, hence, these models can be used to determine the horizontal force required for SZI at,

for example, passive margins. SZI involving the formation of a new plate boundary at a passive margin, so-called newly destructive SZI after Cramer et al. (2020), requires most likely a mechanism that mechanically softens, or weakens, the lithosphere while compressive horizontal forces build up. Several softening mechanisms have been proposed that can facilitate strain localisation of a compressed lithosphere during SZI, such as reaction-induced softening (e.g., White and Knipe, 1978), fluid-induced softening (e.g., Regenauer-Lieb et al., 2001; Dymkova and Gerya, 2013), evolution of fabric and anisotropy (e.g., Montési, 2013) or grain damage (e.g., Bercovici and Ricard, 2012; Mulyukova and Bercovici, 2018). All these mechanisms require knowledge of microscale (i.e., mineral grain scale) or two-phase (solid-fluid) pore-scale processes, which remain poorly constrained and are challenging to upscale for lithosphere models having typically numerical resolutions in the order of a kilometer. A softening mechanism that does not require assumptions of microscale and two-phase processes and that results only from the fundamental law of conservation of energy and the well established temperature dependence of viscous creep of rocks is thermal softening (e.g., Yuen et al., 1978; Regenauer-Lieb and Yuen, 1998). The conversion of dissipative work into heat, so called shear or strain heating, is inherent in all inelastic deformation such as viscous, or rate-dependent, and plastic, or rate-independent deformation. Hence, since viscous creep is thermally activated (e.g., Turcotte and Schubert, 2014), thermal softening may effectively reduce the strength of the viscously deforming regions of the lithosphere and yield to spontaneous formation of shear zones (e.g., Yuen et al., 1978; Regenauer-Lieb and Yuen, 1998; Leloup et al., 1999; Takeuchi and Fialko, 2012; Kiss et al., 2019). Furthermore, all physical processes proposed to explain high-velocity weakening of frictional faults are essentially related to shear heating (e.g., Aharonov and Scholz, 2018). Therefore, we consider here shear heating and associated thermal softening of viscous creep as main softening mechanism during SZI on the lithospheric scale, as has been done in several previous studies (Thielmann and Kaus, 2012; Jaquet and Schmalholz, 2018; Kiss et al., 2020; Auzemery et al., 2020, 2021).

Models for SZI at passive margins consider frequently an initial model configuration with an idealized, ad hoc designed passive margin geometry and associated temperature field (e.g., Auzemery et al., 2020; Kiss et al., 2020). At an idealized passive margin with homogeneous crustal and mantle material properties, Kiss et al. (2020) reported a required horizontal force per unit length of ca.  $37 \text{ TN m}^{-1}$ , indicating that high driving forces are required for shear heating to cause SZI. Such large driving forces, and associated locally high deviatoric stresses, have been used as argument against thermal softening being a feasible mechanism for shear localization (e.g., Platt, 2015). An important step to reduce the driving force necessary for SZI by thermal softening is to consider more realistic passive margin architectures. Including mechanical heterogeneities and numerically modelling the architecture of passive margins prior to convergence, instead of designing these margins ad hoc, Candiotti et al. (2020) and Candiotti et al. (2021) report significantly smaller force magnitudes between 15 and  $18 \text{ TN m}^{-1}$  for thermal softening induced SZI. Although the plate

driving force magnitudes in these models are significantly reduced, a minimum value for horizontal forces required for SZI *via* thermal softening has not been quantified yet in a systematic way. Here, we generate the passive margin architecture with a numerical lithosphere rifting simulation and apply this architecture as initial configuration for convergence simulations to investigate SZI at passive margins (see also Candiotti et al., 2020, 2021, for detailed discussion). Advantages of using a numerically calculated passive margin architecture as initial configuration are that 1) such architecture is thermomechanically feasible and consistent with the applied convergence model, 2) it is isostatically stable and 3) the initial temperature field, including thermal convection in the upper mantle, is consistent with the architecture and applied thermal parameters.

Here, we present two-dimensional (2D) petrological-thermomechanical numerical models that predict SZI at hyperextended passive continental margins. We aim to quantify the minimum horizontal force required for SZI at a passive continental margin *via* thermal softening. Hence, we quantify the resistance to failure of the lithosphere around passive margins under compressive forces during SZI. After SZI we continue modelling convergence and progressive subduction until slab detachment (SD) occurs. Therefore, we also quantify tensile forces, arising due to increasing slab pull, required to fail the lithosphere by SD. With our model we want to test the following hypothesis: The magnitude of the horizontal force required for SZI also controls the force required for detachment of the slab generated by SZI. Therefore, the smaller the force required for SZI, the shorter the slab for which SD occurs. In other words, if the force required for SZI is small, then the initiated subduction zone cannot generate a slab of significant length. To this end, we systematically limit the stresses in the load-bearing layers of the lithosphere (lower crust and mantle lithosphere), because the strength of these layers is a key parameter for successful SZI. Unfortunately, the strength of the lithosphere is difficult to constrain (e.g., Burov and Watts, 2006; Baumann et al., 2014) and often determined by laboratory experiments on olivine, an abundant mineral in the upper mantle, conducted under accelerated deformation conditions and then extrapolated over many orders of magnitude to geological time and deformation scales. In consequence, the actual strength of olivine deforming under geological conditions is currently actively debated (e.g., Demouchy et al., 2013; Idrissi et al., 2016; Hansen et al., 2019; Furstoss et al., 2021). Many recent rock deformation experiments suggest that the strength of olivine is mainly controlled by dislocation glide, or low-temperature plasticity, and is significantly lower than determined in previous laboratory experiments (e.g., Demouchy et al., 2013; Idrissi et al., 2016). However, other studies recently showed that although olivine might be initially weaker than previously thought, strain hardening during increasing rate-dependent plastic deformation might increase its overall strength significantly (e.g., Hansen et al., 2019). Knowledge of the strength of the lithosphere is important because it controls essentially all deformation processes of the lithosphere, such as lithosphere flexure at subduction zones or around seamounts, and of course SZI

and SD as studied here. One aim of our modelling study is, therefore, also to evaluate whether our combined SZI and SD simulations can help in assessing the effective strength of the lithosphere.

Furthermore, we discuss potential implications of our results for the closure and subduction of the Piemonte–Liguria ocean during the formation of the European Alps and potential slab detachment associated with the Alpine continental collision (**Figure 1**). For the Western Alpine orogeny, a wealth of data exists that allowed constraining the tectonic and petrological evolution from SZI at the Adriatic margin, through the closure of the Piemonte–Liguria ocean to the Alpine continental collision potentially involving slab detachment. Thus, the configuration of our numerical models is motivated by tectonic reconstructions for the Alpine orogeny.

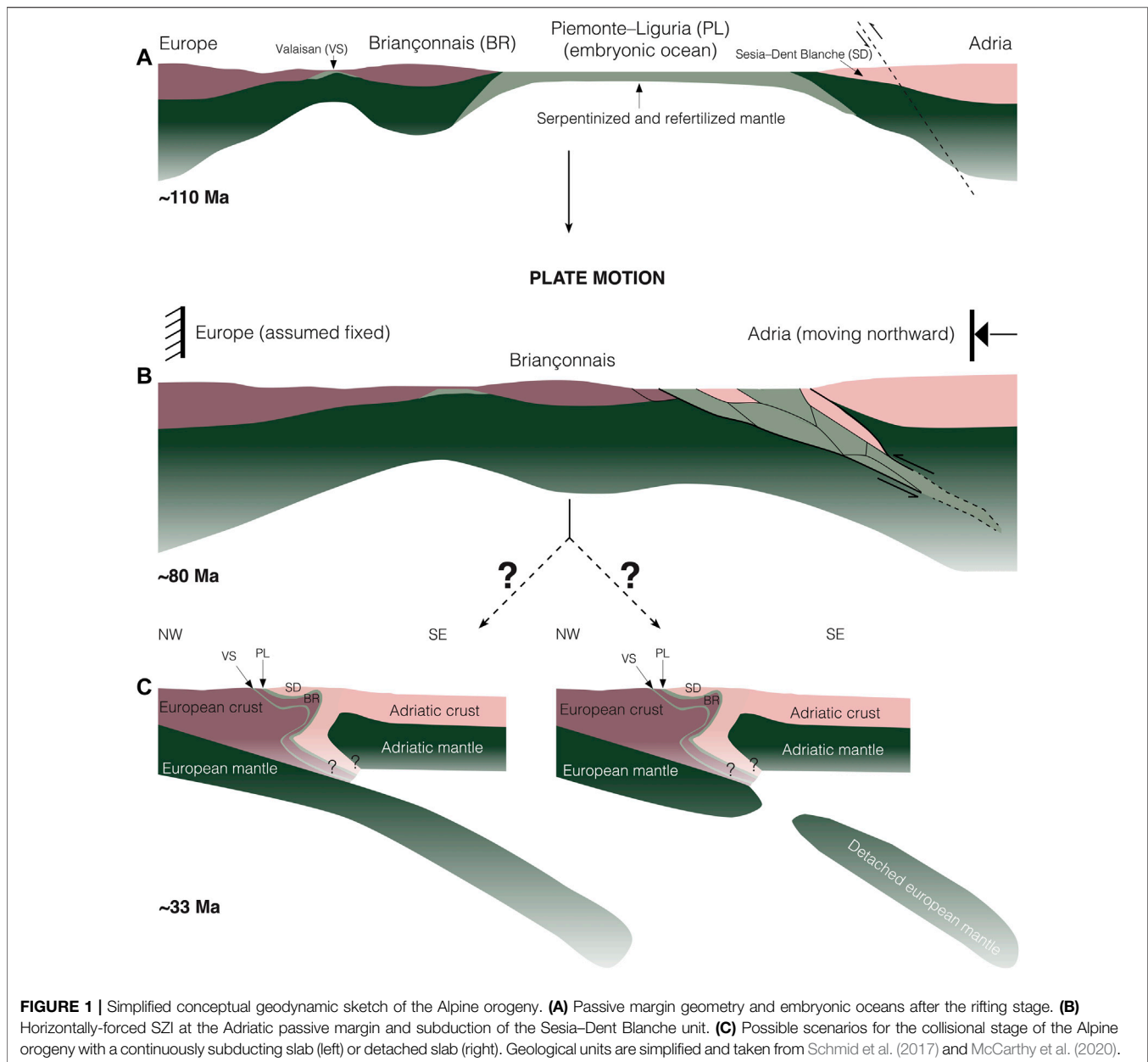
## 2 MODEL

### 2.1 The Alpine Orogeny as Motivation for Our Model Configuration

Here we focus on SZI at magma-poor passive margins that bound embryonic oceans. We define embryonic oceans as marine basins that are small in extent (ca.  $\leq 600$  km) and mainly floored by exhumed mantle and hyperextended continental crust rather than mature oceanic crust (Chenin et al., 2017). Ancient and recent examples of embryonic oceans are, for example, the Piemonte–Liguria ocean (e.g., McCarthy et al., 2020), the present day Ligurian Basin (e.g., Dannowski et al., 2020) and Red Sea (e.g., Chenin et al., 2017). These ocean basins result from slow-to-ultra-slow spreading rift systems, and the architecture and extent of these oceans is similar (Chenin et al., 2017). Mesozoic rifting separated Europe from Adria and terminated at ca. 145 Ma (e.g., Le Breton et al., 2021). This rifting generated the Piemonte–Liguria ocean basin and the two magma-poor passive margins of Europe and Adria (e.g., Handy et al., 2010; McCarthy et al., 2020; Le Breton et al., 2021). The European and Adriatic passive margins were likely hyperextended and bounded the embryonic Piemonte–Liguria ocean (see **Figure 1A**). At ca. 85–80 Ma subduction was presumably initiated within the Adriatic continental margin leading to subduction of the Sesia–Dent Blanche unit (e.g., Manzotti et al., 2014, see **Figure 1B**). Remnants of the Piemonte–Liguria ocean have been incorporated in the Alpine orogenic wedge (e.g., Schmid et al., 2017, see **Figure 1C**). Whether the European slab is detached or still attached to the European plate is currently disputed (e.g., Kästle et al., 2019).

### 2.2 Modelling Approach Involving Geodynamic Cycles

In this study we build upon our previous work presented in Candiotti et al. (2021). Candiotti et al. (2021) presented two-dimensional (2D) petrological-thermomechanical numerical models that simulate several, subsequent geodynamic processes in a single and continuous simulation, including thermal convection in the upper mantle. They modelled 1) the



formation of hyperextended passive continental margins bounding an embryonic ocean, 2) SZI *via* thermal softening during convergence of the ocean-margin system, 3) subduction and closure of an embryonic ocean, 4) formation of a collisional orogen and 5) SD of subducted lithosphere. This Wilson-type cycle of embryonic ocean basins comprised 1) a 50 Myr extension period, 2) a 60 Myr cooling period between the extension and convergence phase and 3) a ca. 70 Myr convergence period. Candiotti et al. (2021) applied this cycle to the opening and closure of the Piemonte-Liguria ocean and the subsequent formation of the European western Alps (e.g., McCarthy et al., 2020). They mainly focused on the competition between buoyancy and shear forces during the collisional stage of the

orogen. When shear forces dominate the collisional stage of the orogen, wedge formation without deep subduction of continental crustal material occurred. When buoyancy forces were equally important as shear forces, Candiotti et al. (2021) observed deep subduction and exhumation of continental units. The mechanical boundary velocities and the duration of the deformation periods they applied were motivated by plate motion reconstructions from the European and Adriatic plate during the past ca. 180 Myr (e.g., Le Breton et al., 2021). Complementary to their results, we here focus on the subduction stage. Especially, we aim at quantifying the minimum force required for SZI and the role of lithospheric strength in the kind of models presented by Candiotti et al. (2021). Note, that we refer to time as the

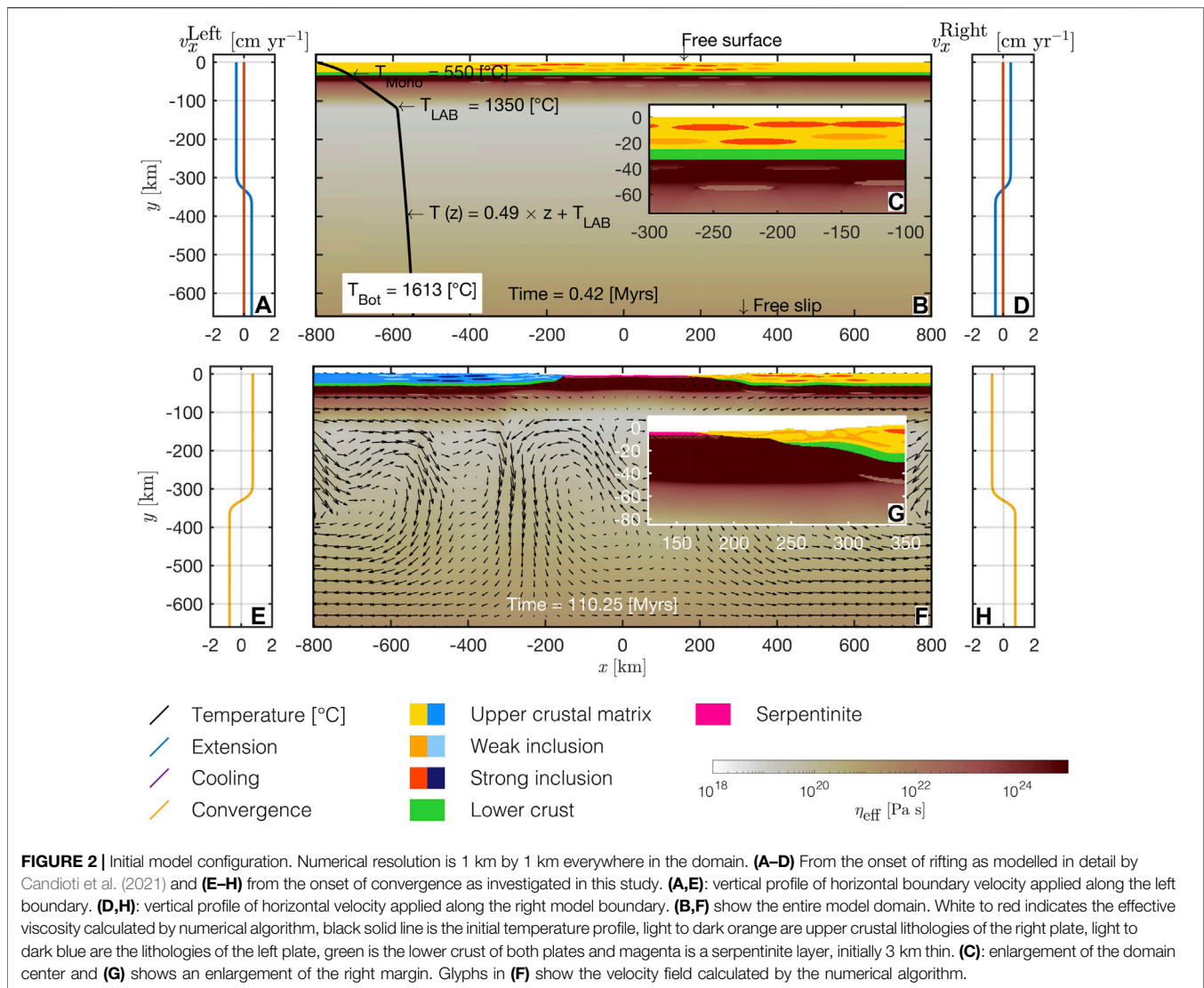


**FIGURE 2 |** Initial model configuration. Numerical resolution is 1 km by 1 km everywhere in the domain. **(A–D)** From the onset of rifting as modelled in detail by Candiotti et al. (2021) and **(E–H)** from the onset of convergence as investigated in this study. **(A,E)**: vertical profile of horizontal boundary velocity applied along the left boundary. **(D,H)**: vertical profile of horizontal velocity applied along the right model boundary. **(B,F)** show the entire model domain. White to red indicates the effective viscosity calculated by numerical algorithm, black solid line is the initial temperature profile, light to dark orange are upper crustal lithologies of the right plate, light to dark blue are the lithologies of the left plate, green is the lower crust of both plates and magenta is a serpentine layer, initially 3 km thin. **(C)**: enlargement of the domain center and **(G)** shows an enlargement of the right margin. Glyphs in **(F)** show the velocity field calculated by the numerical algorithm.

simulated physical time and its unit is Myr. Whenever we refer to actual geological time, we use the unit Ma. **Figures 2A–D** shows the initial configuration used by Candiotti et al. (2021) to model this type of Wilson cycle. A detailed justification of the initial conditions, a full description of the entire model evolution as well as in depth information on the implementation of boundary conditions, petrological-thermomechanical coupling and surface processes (i.e., sedimentation and erosion) is given in the open-access article of Candiotti et al. (2021). The models we present here start from the configuration predicted at 110 Myr (end of cooling period) in model history by the reference model of Candiotti et al. (2021) (see **Figures 2E–H**). Similar to the study of Candiotti et al. (2021), we parameterize a serpentinisation front propagating across the top 3 km of exhumed mantle material in the embryonic oceanic basin before the onset of convergence. Because of ultra-slow spreading rates, no significant mid-ocean ridge with active magmatism is formed. Therefore, embryonic oceans often lack a mature Penrose-type oceanic crust (e.g.,

McCarthy et al., 2020). Instead, the subcontinental mantle is exhumed to the surface and in contact with the sea-water. Thus, serpentinisation is likely significant in embryonic ocean basins and presumably plays an important role during subduction of embryonic oceans (e.g., McCarthy et al., 2020). In our models, convergence is induced by applying a constant absolute boundary horizontal velocity of  $1.5 \text{ cm yr}^{-1}$ . To quantify the minimum driving force and assess the strength of embryonic oceanic lithosphere, we employ a parameterized stress limiter in the mantle lithosphere and the lower crust. In addition to the applied pressure-sensitive Drucker-Prager plastic stress limiter function, this stress limiter is independent on pressure and is used here as a controlling parameter for the plate strength. We systematically tested stress limits of 10, 50, 100, 150, 200, 300, 500 MPa, and 500 GPa. Employing a value of 500 GPa deactivates the stress limiter in the reference model, named NOSLIM hereafter. In addition to the reference model, we here report results for models employing stress limits of 100, 200 and

300 MPa, named SLIM100, SLIM200 and SLIM300 hereafter. These models predict end-member dynamics for subduction initiation and the evolving subduction zone. To test the impact of shear heating and associated thermal softening on SZI we also performed the two simulations SLIM300 and NOSLIM without shear heating.

## 2.3 Governing Equations

We consider incompressible materials that slowly creep (no inertia) under gravity and boundary tractions. The applied numerical algorithm solves the continuity equation, the equation for the conservation of momentum and the heat transfer equation in a two-dimensional Cartesian coordinate system, which are given by:

$$\frac{\partial v_i}{\partial x_i} = 0 \quad (1)$$

$$\frac{\partial \sigma_{ij}}{\partial x_j} = -\rho g_i \quad (2)$$

$$\rho c_p \frac{DT}{Dt} = \frac{\partial}{\partial x_i} \left( k \frac{\partial T}{\partial x_i} \right) + H_A + H_D + H_R, \quad (3)$$

where  $i$  and  $j$  are spatial indices and repeated indices are summed,  $v$  is velocity and  $x$  is the spatial coordinate,  $\sigma$  is the total stress tensor,  $\rho$  is density and  $g = [0; -9.81]$  is a vector including the gravitational acceleration. The density is a function of temperature,  $T$ , pressure,  $P$ , and a given bulk rock composition,  $C$ , which is precomputed using a thermodynamic software package (Perple\_X Connolly, 2005, 2009). We, thus, include large density variations resulting from mineral phase transitions. For example, at a lithostatic pressure and a temperature corresponding to a depth of ca. 410 km, the olivine–wadsleyite phase transition results in a density increase of ca.  $150 \text{ kg m}^{-3}$  (see Candiotti et al., 2020, **Figures 2B,E**). Such an increase might significantly impact on the subduction dynamics. A detailed description of the implementation of petrological-thermomechanically coupled processes and the applied chemical composition of the model units is given in the two open-access publications Candiotti et al. (2020) and Candiotti et al. (2021). In **Eq. 3**,  $c_p$  is heat capacity at constant  $P$ ,  $D/Dt$  is the material time derivative,  $k$  is thermal conductivity and  $H_R$  comprise source terms resulting from radiogenic heat production. We include source terms resulting from adiabatic processes (Extended Boussinesq Approximation, e.g., Candiotti et al., 2020, for detailed justification),  $H_A = T \alpha v_y g_p$ , where  $\alpha$  is the coefficient of thermal expansion and  $v_y$  is the vertical component of velocity. Further, we consider contributions from the conversion of rate-dependent and rate-independent mechanical processes into heat,  $H_D = \tau_{ij} (\dot{\epsilon}_{ij} - \dot{\epsilon}_{ij}^{\text{ela}})$ , where  $\dot{\epsilon}$  is the total deviatoric strain rate tensor and  $\dot{\epsilon}^{\text{ela}}$  denotes the strain rate resulting from elastic deformation. The total stress tensor is decomposed into a pressure and a deviatoric part as

$$\sigma_{ij} = -P \delta_{ij} + 2 \eta^{\text{eff}} \dot{\epsilon}_{ij}^{\text{eff}} \quad (4)$$

$$\delta_{ij} = \begin{cases} 0 & , i \neq j \\ 1 & , i = j, \end{cases} \quad (5)$$

where  $\delta_{ij}$  is the Kronecker-Delta,  $\eta^{\text{eff}}$  is the effective viscosity,  $\dot{\epsilon}^{\text{eff}}$  is the effective deviatoric strain rate tensor,

$$\dot{\epsilon}_{ij}^{\text{eff}} = \left( \dot{\epsilon}_{ij} + \frac{\tau_{ij}^o}{2G\Delta t} \right), \quad (6)$$

where  $G$  is shear modulus,  $\Delta t$  is the time step,  $\tau^o$  are the deviatoric stress tensor components of the preceding time step. We consider visco-elasto-plastic deformation and additively decompose (so-called Maxwell model) the total deviatoric strain rate tensor into contributions from rate-dependent plastic deformation (i.e., effectively viscous behaviour by dislocation, diffusion and Peierls creep), elastic and rate-independent (brittle) plastic deformation as

$$\dot{\epsilon}_{ij} = \dot{\epsilon}_{ij}^{\text{ela}} + \dot{\epsilon}_{ij}^{\text{pla}} + \dot{\epsilon}_{ij}^{\text{dis}} + \dot{\epsilon}_{ij}^{\text{dif}} + \dot{\epsilon}_{ij}^{\text{Pei}}. \quad (7)$$

The viscosity for dislocation, diffusion and Peierls creep are a function of the respective second strain rate tensor invariant,  $\dot{\epsilon}_{\text{II}}^{\text{dis,dif,Pei}} = \sqrt{\frac{1}{2} (\dot{\epsilon}_{ij}^{\text{dis,dif,Pei}})^2}$ . The dislocation and diffusion creep viscosity are computed as

$$\eta^{\text{dis,dif}} = \frac{2^{1-n}}{3^{2n}} A^{-\frac{1}{n}} (\dot{\epsilon}_{\text{II}}^{\text{dis,dif}})^{\frac{1}{n}-1} d^m \exp\left(\frac{Q+PV}{nRT}\right) (f_{\text{H}_2\text{O}})^{-\frac{r}{n}}, \quad (8)$$

where  $d$  is grain size and the ratio in front of the prefactor  $A$  results from the conversion of experimentally derived flow laws into a tensor formulation of these flow laws (e.g., Schmalholz and Fletcher, 2011). The quantities  $A$ ,  $n$ ,  $m$ ,  $Q$ ,  $V$ ,  $f_{\text{H}_2\text{O}}$  and  $r$  are experimentally determined material parameters which are characteristic for each creep law (see **Table 1**). To increase the readability we have omitted the superscripts “dif/dis” for these parameters. Note that for diffusion creep the  $n = 1$  and for dislocation creep  $m = 0$ . Hence, dislocation and diffusion creep are essentially insensitive to grain size and strain rate, respectively. We further include the experimentally derived Peierls flow law by Goetze and Evans (1979) expressed in the regularized form of Kameyama et al. (1999) and calculate the Peierls viscosity as

$$\eta^{\text{Pei}} = \frac{2^{\frac{1-s}{s}}}{3^{\frac{1+s}{2s}}} \hat{A} (\dot{\epsilon}_{\text{II}}^{\text{Pei}})^{\frac{1}{s}-1}, \quad (9)$$

employing an effective stress exponent

$$s = 2 \gamma \frac{Q}{RT} (1 - \gamma). \quad (10)$$

$\hat{A}$  in **Eq. 9** is calculated as

$$\hat{A} = \left[ A^{\text{Pei}} \exp\left(-\frac{Q(1-\gamma)^2}{RT}\right) \right]^{-\frac{1}{s}} \gamma \sigma^{\text{Pei}}, \quad (11)$$

where  $A^{\text{Pei}}$ ,  $\gamma$  and  $\sigma^{\text{Pei}}$  are material parameters. We control rate-independent (brittle) plastic deformation by a deviatoric stress limiter function

$$F = \tau_{\text{II}} - \tau^{\text{eq}} \quad (12)$$

$$\tau^{\text{eq}} = \begin{cases} P \sin \varphi + C \cos \varphi & , P \sin \varphi + C \cos \varphi < S \\ S & , P \sin \varphi + C \cos \varphi \geq S, \end{cases} \quad (13)$$

**TABLE 1** | Physical parameters used in the numerical simulations.

Model Unit	Rheology (reference)	$k$ [ $\text{W m}^{-1} \text{K}^{-1}$ ]	$H_R$ [ $\text{W m}^{-3}$ ]	$C$ [Pa]	$\varphi$ [°]	
Crustal matrix <sup>a</sup>	Westerly Granite Hansen and Carter (1983)	2.25	$1.0200 \times 10^{-6}$	$1 \times 10^7$	30	
Weak inclusion <sup>a</sup>	Wet Quartzite Ranalli (1995)	2.25	$1.0200 \times 10^{-6}$	$1 \times 10^6$	5	
Strong inclusion <sup>a</sup>	Maryland Diabase Mackwell et al. (1998)	2.25	$1.0200 \times 10^{-6}$	$1 \times 10^7$	30	
Calcite <sup>a</sup>	Calcite Schmid et al. (1977)	2.37	$0.5600 \times 10^{-6}$	$1 \times 10^7$	30	
Mica <sup>a</sup>	Mica Kronenberg et al. (1990)	2.55	$2.9000 \times 10^{-6}$	$1 \times 10^7$	15	
Lower crust <sup>b</sup>	Wet Anorthite Rybacki and Dresen (2004)	2.25	$0.2600 \times 10^{-6}$	$1 \times 10^7$	30	
Strong mantle <sup>c</sup>	Dry Olivine Hirth and Kohlstedt (2003)	2.75	$2.1139 \times 10^{-8}$	$1 \times 10^7$	30	
Weak mantle <sup>c</sup>	Wet Olivine Hirth and Kohlstedt (2003)	2.75	$2.1139 \times 10^{-8}$	$1 \times 10^7$	30	
Serpentinite <sup>d</sup>	Antigorite Hilairet et al. (2007)	2.75	$2.1139 \times 10^{-8}$	$1 \times 10^7$	25	
Dislocation creep	$A$ [ $\text{Pa}^{-n-r} \text{m}^m \text{s}^{-1}$ ]	$m$ [ ]	$n$ [ ]	$Q$ [ $\text{J mol}^{-1}$ ]	$V$ [ $\text{m}^3 \text{mol}^{-1}$ ]	$r$ [ ]
Crustal matrix	$3.1623 \times 10^{-26}$	0.0	3.3	$186.5 \times 10^3$	$0.00 \times 10^{-6}$	0.0
Weak inclusion	$5.0717 \times 10^{-18}$	0.0	2.3	$154 \times 10^3$	$0.00 \times 10^{-6}$	0.0
Strong inclusion	$5.0477 \times 10^{-28}$	0.0	4.7	$485 \times 10^3$	$0.00 \times 10^{-6}$	0.0
Calcite	$1.5849 \times 10^{-25}$	0.0	4.7	$297 \times 10^3$	$0.00 \times 10^{-6}$	0.0
Mica	$1.0000 \times 10^{-138}$	0.0	18.0	$51.0 \times 10^3$	$0.00 \times 10^{-6}$	0.0
Lower crust	$3.9811 \times 10^{-16}$	0.0	3.0	$356 \times 10^3$	$0.00 \times 10^{-6}$	0.0
Strong mantle	$1.1000 \times 10^{-16}$	0.0	3.5	$530 \times 10^3$	$14.0 \times 10^{-6}$	0.0
Weak mantle <sup>e</sup>	$5.6786 \times 10^{-27}$	0.0	3.5	$480 \times 10^3$	$11.0 \times 10^{-6}$	1.2
Serpentinite	$4.4738 \times 10^{-38}$	0.0	3.8	$8.90 \times 10^3$	$3.20 \times 10^{-6}$	0.0
Diffusion creep <sup>f</sup>	$A$ [ $\text{Pa}^{-n-r} \text{m}^m \text{s}^{-1}$ ]	$m$ [ ]	$n$ [ ]	$Q$ [ $\text{J mol}^{-1}$ ]	$V$ [ $\text{m}^3 \text{mol}^{-1}$ ]	$r$ [ ]
Strong mantle	$1.5000 \times 10^{-15}$	3.0	1.0	$375 \times 10^3$	$7.5 \times 10^{-6}$	0.0
Weak mantle <sup>e</sup>	$2.5000 \times 10^{-23}$	3.0	1.0	$375 \times 10^3$	$7.0 \times 10^{-6}$	1.0
Peierls creep	$A^{\text{Pei}}$ [ $\text{s}^{-1}$ ]	$Q$ [ $\text{J mol}^{-1}$ ]	$V$ [ $\text{m}^3 \text{mol}^{-1}$ ]	$\sigma^{\text{Pei}}$ [Pa]	$\gamma$ [ ]	
Mantle <sup>g</sup>	$5.7000 \times 10^{11}$	$540 \times 10^3$	$0.0 \times 10^{-6}$	$8.5 \times 10^9$	0.1	

Constant parameters: A heat capacity  $c_p = 1,050 \text{ [J kg}^{-1} \text{K}^{-1}]$  is employed for all phases.

<sup>a,b,c</sup>A constant shear modulus  $G = 2 \times 10^{10} \text{ [Pa]}$  is used.

<sup>d</sup>A constant shear modulus  $G = 1.81 \times 10^{10} \text{ [Pa]}$  is used.

<sup>e</sup>A water fugacity  $f_{\text{H}_2\text{O}} = 1.0 \times 10^9 \text{ [Pa]}$  is used. For all other phases  $f_{\text{H}_2\text{O}} = 0.0 \text{ [Pa]}$ .

<sup>f</sup>A constant grain size  $d = 1 \times 10^{-3} \text{ [m]}$  is used.

<sup>g</sup>Reference: Goetze and Evans (1979) regularized by kameyama1999thermal. These parameters are used for both strong and weak mantle rheology.

where,  $\tau_{\text{II}} = \sqrt{\frac{1}{2}(\tau_{ij})^2}$  is the second invariant of the deviatoric stress tensor,  $\varphi$  is the internal angle of friction,  $C$  is the cohesion and  $S$  is a stress limiter which is a parameter that is not experimentally derived but a variable used to control the material strength. The plastic viscosity at the equivalent deviatoric stress,  $\tau^{\text{eq}}$ , is computed as

$$\eta^{\text{vep}} = \frac{\tau^{\text{eq}}}{2\dot{\epsilon}_{\text{II}}^{\text{eff}}}, \quad (14)$$

where  $\dot{\epsilon}_{\text{II}}^{\text{eff}} = \sqrt{\frac{1}{2}\dot{\epsilon}_{ij}^{\text{eff}}\dot{\epsilon}_{ij}^{\text{eff}}}$ . In Eq. 4, the effective viscosity is either the quasi-harmonic average of the visco-elastic contributions

$$\eta^{\text{eff}} = \begin{cases} \left( \frac{1}{G\Delta t} + \frac{1}{\eta^{\text{dis}}} + \frac{1}{\eta^{\text{dif}}} + \frac{1}{\eta^{\text{pei}}} \right)^{-1}, & F < 0 \\ \eta^{\text{vep}}, & F \geq 0 \end{cases} \quad (15)$$

or is equal to  $\eta^{\text{vep}}$ . Advection of material is performed using a marker-and-cell technique (Gerya and Yuen, 2003) and we compute rigid body rotation of stresses analytically (see also Candiotti et al., 2021, for a more detailed description of the algorithm). A marker chain and a stabilisation algorithm (Duretz et al., 2011b, 2016) is employed to allow for dynamic evolution of topography. Surface processes, namely erosion and sedimentation, are parameterized in the model. In case, the

newly computed topography falls below a sedimentation level of  $z = -5 \text{ km}$  it is corrected back to the sedimentation level. The resulting gap between the newly computed topographic level and the sedimentation level is filled instantaneously with markers describing a calcite or a mica rheology. The rheology of the sediment markers alternates every 2 Myr. In case the newly computed topography rises above an erosion level of  $z = 2 \text{ km}$ , the topographic level is corrected downward. The distance of correction is calculated by multiplying the current time increment,  $\Delta t$ , by a constant erosion velocity of  $0.5 \text{ mm yr}^{-1}$ . All material parameters used in the models presented here are listed in Table 1.

## 2.4 Calculation of Plate Driving Forces and Slab-Pull-Force Estimate

Here,  $F_D = 2 \times \tau_{\text{II}}^{\text{avg}}$  is used as a representative value for the horizontal driving force per unit length. Close to the lateral model boundaries, where  $F_D$  is calculated, the smallest principal stress is vertical and is close to the lithostatic pressure, and the maximal principal stress is approximately horizontal. Therefore,  $F_D$  is a representative estimate for the plate driving force (e.g., Schmalholz et al., 2014, 2019). First, the vertical integral of  $\tau_{\text{II}}(x, y)$  is calculated at the different horizontal positions of the numerical grid as

$$\bar{\tau}_{II}(x) = \int_b^a \tau_{II}(x, y) dy, \quad (16)$$

where  $a$  is the topographic level at each horizontal grid point and  $b = -660$  km is the bottom coordinate of the model domain. The values of  $\bar{\tau}_{II}(x)$  are then averaged horizontally inside two regions of 100 km width located at the two lateral model sides. This horizontally averaged, vertically integrated stress is termed  $\bar{\tau}_{II}^{avg}$ . The reader is referred to Candiotti et al. (2020) for further detail.

We further estimate the slab-pull force per unit length by calculating the effective body force of the subducting slab. This body force,  $F_{SP}$ , is computed as the difference between densities of all material that is 1) enclosed horizontally within  $-700 \leq x \leq 700$  km of the domain, 2) colder than  $T \leq 1,300^\circ\text{C}$  and 3) subducted below  $y = -160$  km and a vertical reference density profile. This reference profile is obtained from the last time step of the cooling period of model NOSLIM by averaging horizontally all material densities at each vertical grid level below  $y = -160$  km over the entire horizontal domain. This reference density is also used to compute the density difference,  $\Delta\rho$ , induced by a phase transition. The body force is then calculated as follows:

$$F_{SP} = \int_{\Omega} \Delta\rho g d\Omega, \quad (17)$$

where  $\Delta\rho$  is the aforementioned density difference integrated over the area  $\Omega$  covered by material matching the three criteria defined above. This is a maximum estimate for the slab-pull force, because the surrounding mantle material exerts shear stresses on the slab surface which resist subduction. Assuming shear stress magnitudes of 1–10 MPa along the bottom and top of a ca. 500 km long slab results in force magnitudes between 1 and 10 TN  $\text{m}^{-1}$ , respectively, acting against the slab pull force due to buoyancy only. Therefore, the natural, effective slab pull force magnitudes including the shear resistance from the surrounding mantle are likely lower than the ones reported here (see also Turcotte and Schubert, 2014). However, the relative evolution of  $F_{SP}$  likely remains as reported here.

### 3 RESULTS

In this section we first report the results of the reference model without stress limiter, termed NOSLIM, and compare them to the models with different stress limits afterwards. We compare the stage of SZI, the evolution of plate driving and approximated slab pull forces as well as the dynamics of SD. We refer to the model passive margins on the left and right side of the model as left and right margin from here onward.

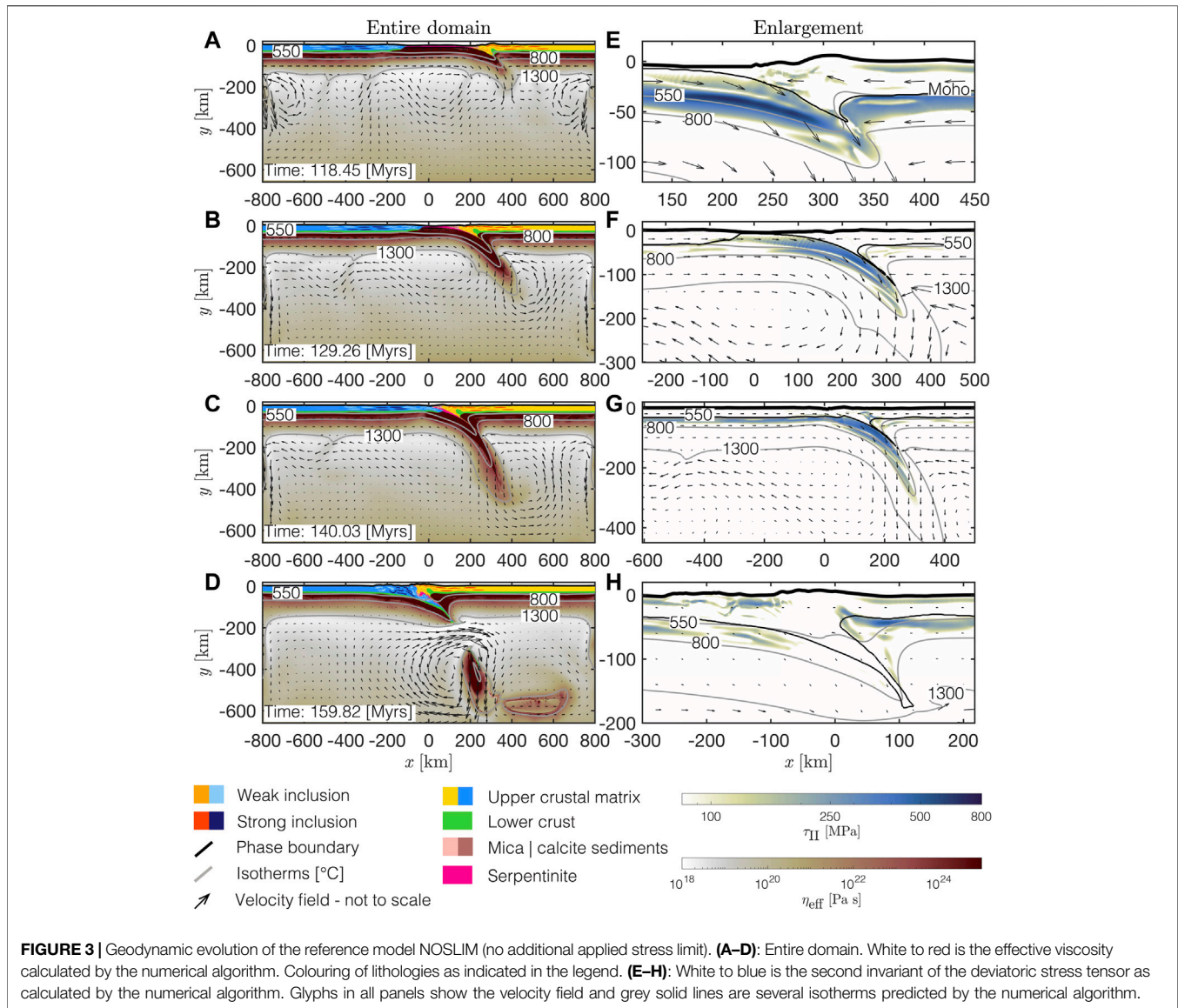
#### 3.1 Geodynamic Evolution of the Reference Model NOSLIM

Convergence is started at 110 Myr in model history. Subduction initiates at ca. 113 Myr at the transition zone between the

proximal and the necking domain within the mantle lithosphere of the right margin (Figures 3A,E). SZI occurs at a region where no serpentinite is present which indicates that the initially horizontal serpentinite layer is not important for SZI. This conclusion is also supported by the findings of Candiotti et al. (2021), who report successful SZI with and without a serpentinite layer in similar numerical models. Maximal bending stresses within the lithosphere of the subducting and overriding plate are ca. 500–700 MPa and limited to a 10–25 km thin layer (Figure 3E). Until ca. 129 Myr, large portions of the serpentinite are sheared off the subducting slab (Figure 3B). The values for stresses decrease below ca. 100 MPa within the overriding plate and remain at ca. 250–400 MPa where the subducting plate is bent below the overriding plate (Figures 3F,G). This stage marks the successful SZI in this simulation. The embryonic ocean basin is closed at ca. 140 Myr in model history. At this stage, the serpentinite material has largely been sheared off the subducting plate and reorganized along the plate interface (Figure 3C). A thrust wedge has formed at ca. 160 Myr and a large part of the subducting slab has been detached from the subducting plate (Figure 3D). The values of deviatoric stresses within the thrust wedge remain between ca. 100–250 MPa (e.g.,  $-200 \leq x \leq -100$  km and  $y > -30$  km in Figure 3H).

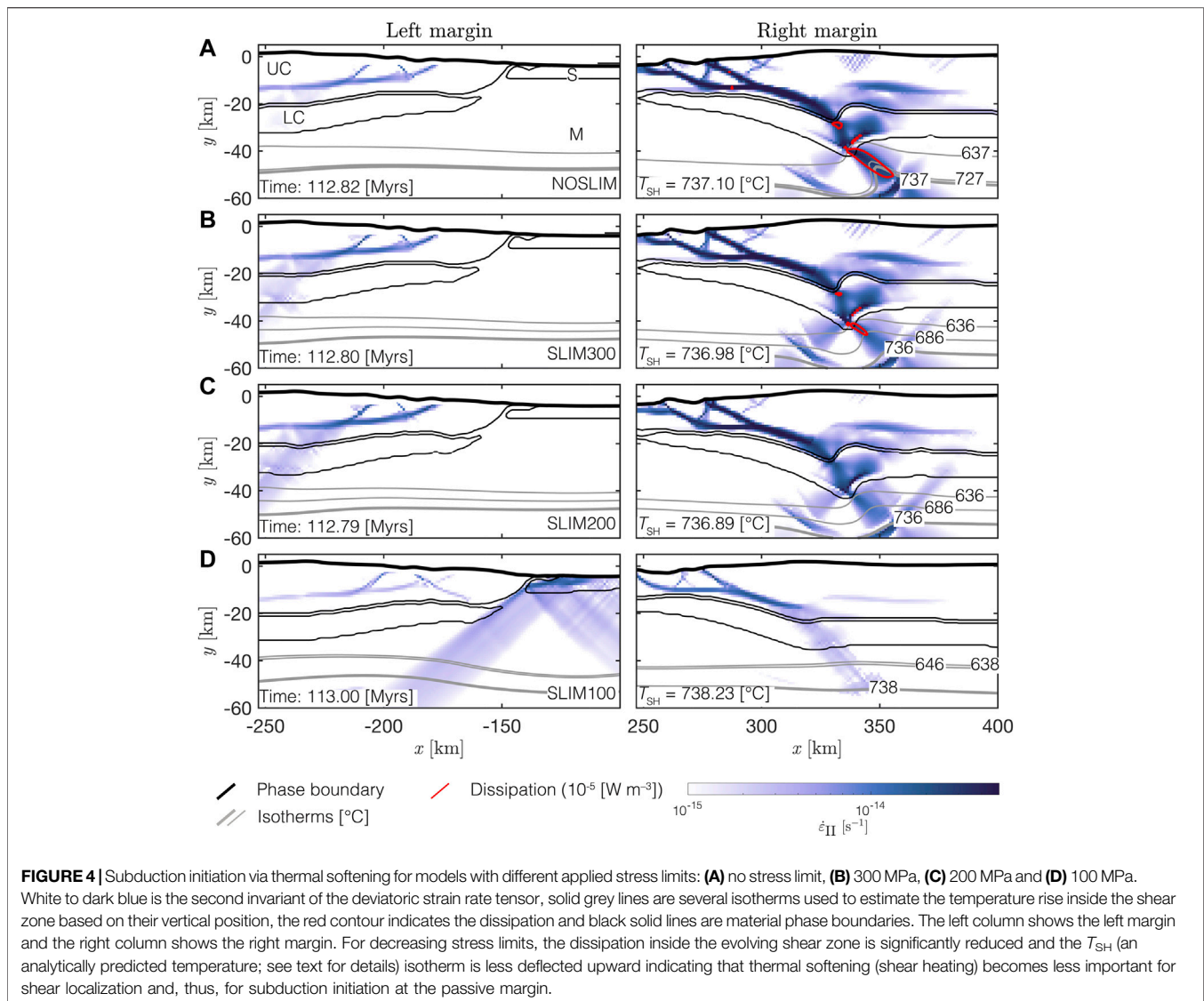
#### 3.2 Subduction Initiation at Hyperextended Continental Margins

Figure 4 shows the stage of SZI in the different models. In the reference model, NOSLIM, and in SLIM300 a shear zone forms below the right margin (blue region in right column of Figures 4A,B). Values for dissipative heating inside the shear zone are above  $10^{-5} \text{ W m}^{-3}$  (red contour line in Figures 4A,B) and the temperature inside the evolving shear zone increases compared to the surrounding ambient mantle temperature. This temperature increase is indicated by the geometry of the isotherms which are in shallower depth inside the shear zone compared to the corresponding isotherms to the left and right side of the shear zone. By comparing the vertical position of the grey isotherms in Figures 4A,B, one can estimate the temperature rise inside the shear zone assuming that before shear zone formation the isotherms were approximately horizontal, like in the corresponding left margins. For example, at the right margin of model NOSLIM, the isotherm for  $727^\circ\text{C}$  inside the shear zone is in approximately the same depth as the horizontal isotherm for  $637^\circ\text{C}$  to the left of the shear zone. Therefore, in NOSLIM the temperature rises by ca.  $90^\circ\text{C}$  and in SLIM300 by ca.  $50^\circ\text{C}$ , using the same estimate based on isotherm geometries. Kiss et al. (2019) showed that a small temperature increase of only ca.  $50^\circ\text{C}$  already can cause strain localization by thermal softening. Compared to models NOSLIM and SLIM300, less dissipative heat is generated by the shear zone forming in model SLIM200. The temperature rise inside the shear zone of model SLIM200 is still ca.  $50^\circ\text{C}$ , which is comparable to model SLIM300. In SLIM100 the heat generated by the conversion of mechanical work into heat is insignificant and the temperature inside the shear zone rises by less than  $10^\circ\text{C}$  (compare Figures 4A,B to Figures 4C,D). Figure 5



shows which regions in the model exhibit only rate-independent plastic, or brittle, deformation (highlighted in blue) and which regions exhibit elastic or rate-dependent plastic, or ductile, deformation (highlighted in white, see **Section 2.3** for calculation). In contrast to the ductile (white regions in **Figures 5A,B**) shear zones formed in NOSLIM and SLIM300, the shear zones in SLIM200 and SLIM100 are mainly formed due to brittle deformation (blue regions in **Figures 5C,D**). The reason is that in SLIM200 and SLIM100 the stress limits are lower and, hence, the regions in which stresses exceed the stress limit (i.e., here the brittle region) become larger. Further, brittle shear zones also form below the left margin in SLIM100 (**Figure 4D** and **Figure 5D**). In consequence, the subduction zone in SLIM100 evolves completely different compared to the subduction zone in SLIM300. Subduction in SLIM100 is initiated below the opposite margin (**Figures 6A,B**) and the slab is

subducted much slower (compare depth of slab tip in the left and right column of **Figure 6C**). The detachment of the slab occurs approximately at the same depth in SLIM100 and SLIM300, but much later in SLIM100 compared to SLIM300 (156 and 150 Myr, respectively, **Figure 6D**). We consider the slab as detached when the distance between the 1,300°C isotherms bounding the slab is less than 10 km. The slab in model SLIM300 is much longer than it is thick, thus resembling the typical rectangular cross-sectional shape of a slab. In contrast, the shape of the slab in SLIM100 resembles more the cross-sectional shape of a lithospheric droplet rather than a subducting slab (compare left and right panel **Figure 6D**). The deformation behaviour observed in SLIM100 is very similar to the so-called drip-off mode described in the numerical simulations of Thielmann and Kaus (2012). This deformation behaviour does not correspond to the subduction of a coherent plate-like slab.

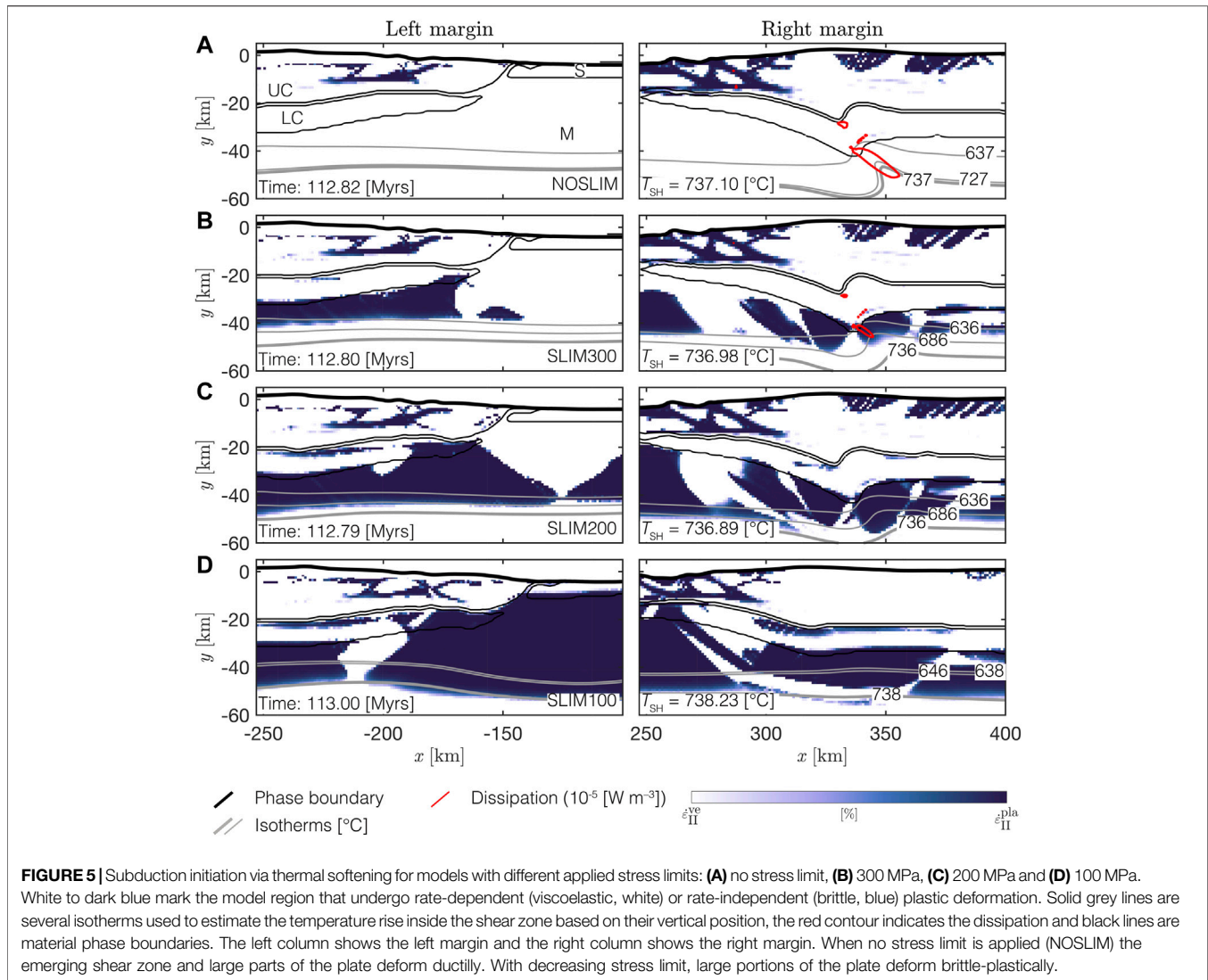


As shown above, the maximum temperature increase associated with the formation of shear zones is less than 100°C. It is, therefore, difficult to isolate the temperature increase exclusively caused by shear heating because of the simultaneously ongoing temperature advection and conduction. To clearly show that the shear zones, causing SZI in our models, are due to shear heating and associated thermal softening, we have performed two additional simulations of NOSLIM and SLIM300 in which we have deactivated the shear heating (**Figure 7**). This deactivation was done by setting the term  $H_D$  in **Eq. 3** to zero. When shear heating is deactivated (see right column in **Figure 7**) SZI is not successful. Instead, buckling and thickening in the regions of the two margins is the dominant deformation behaviour of the lithosphere. Therefore, the four simulations NOSLIM and SLIM300 with and without shear heating clearly show that shear heating is causing SZI in our models. Consequently,

other model features such as the mechanical heterogeneities, mimicked by initial elliptical heterogeneities, or the serpentinite layer are not able to cause SZI.

### 3.3 Evolution of Horizontal Driving Force and Approximate Slab Pull Force

In **Figure 8** we report the evolution of the plate driving forces per unit length,  $F_D$ , and an approximate estimate for the slab pull force per unit length,  $F_{SP}$ , over time. The magnitude of  $F_D$  increases to ca. 18  $\text{TN m}^{-1}$  in NOSLIM, ca. 15  $\text{TN m}^{-1}$  in SLIM300 and ca. 12  $\text{TN m}^{-1}$  in SLIM200 between the onset of convergence and ca. 113 Myr (**Figure 8A**). A maximum  $F_D = 14 \text{ TN m}^{-1}$  is reached at ca. 122 Myr in SLIM200. Between ca. 113 and 114 Myr, values for  $F_D$  decrease in NOSLIM and SLIM300 and remain relatively constant in SLIM200. In NOSLIM, SLIM300 and SLIM200, the values for  $F_D$  overall decrease to ca. 10  $\text{TN m}^{-1}$  between ca. 130 Myr and ca. 135 Myr. In SLIM100 the magnitude of  $F_D$



continuously increases to ca.  $10 \text{ TN m}^{-1}$  until ca. 122 Myr in model history (blue solid line in **Figure 8A**).

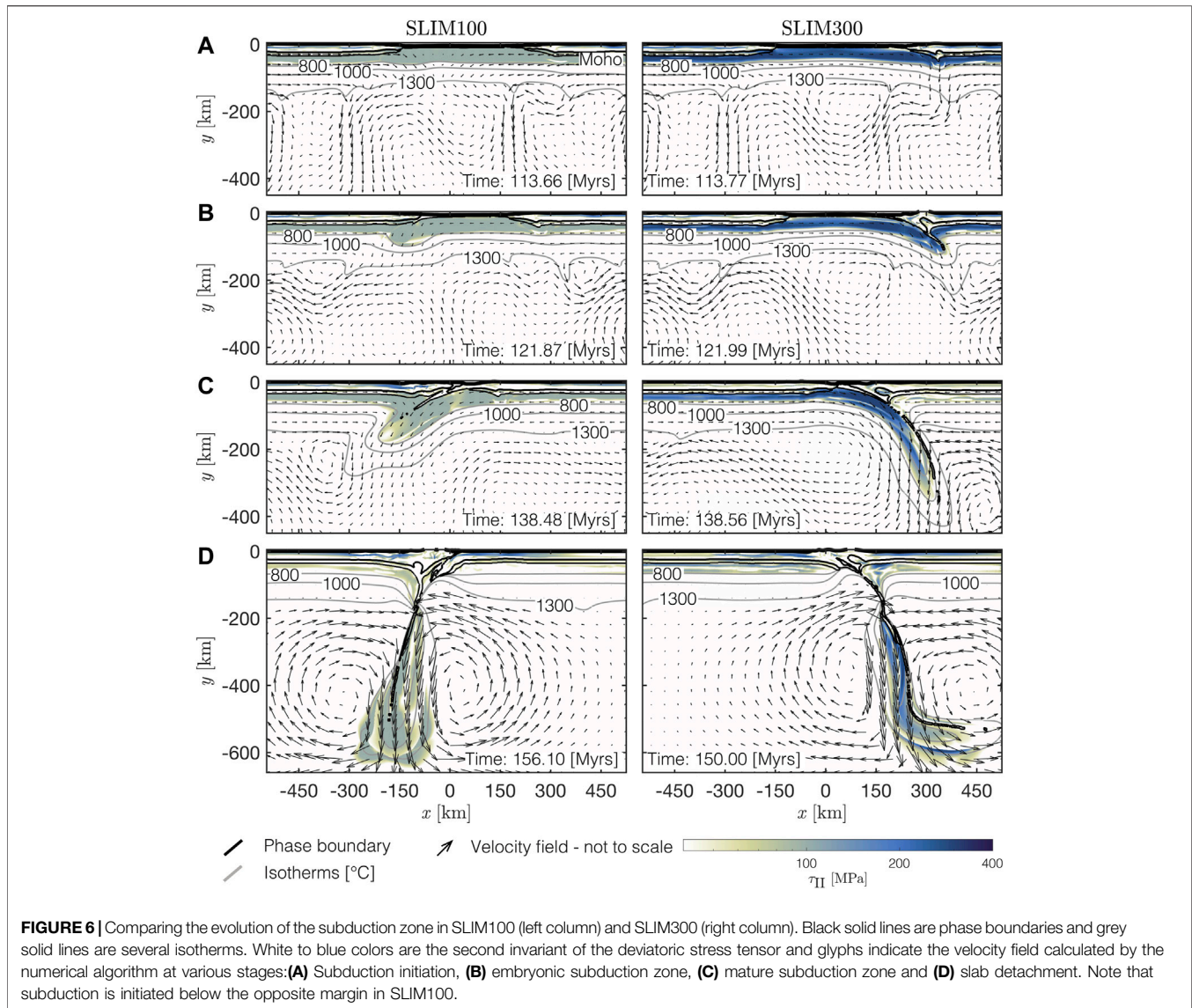
The density within the subducting slab increases by up to  $150 \text{ kg m}^{-3}$  compared to the ambient mantle density structure when it transects  $y = -410 \text{ km}$  (**Figures 8D–F**). The reason for this increase in density is the olivine–wadsleyite phase transition. Due to a positive Clapeyron slope (i.e., the change in temperature–pressure space), this phase transition occurs at shallower depths for cold material than for hot material. Therefore, the phase transition is deflected upward inside the cold subducting slabs (see **Figures 8D–F**) and induces an additional pull force. A gradual increase in  $F_{\text{SP}}$  until the onset of necking in the subducting slab (left edge of grey rectangles in **Figure 8B**, see also stages in **Figures 8D–F**) is observed in all models. This stage is reached after ca. 141 Myr in SLIM200, ca. 150 Myr in SLIM300 and ca. 158 Myr in NOSLIM. The corresponding magnitudes are  $F_{\text{SP}} \approx 15 \text{ TN m}^{-1}$  in SLIM200,  $F_{\text{SP}} \approx 25 \text{ TN m}^{-1}$  in SLIM300 and  $F_{\text{SP}} \approx 35 \text{ TN m}^{-1}$  in NOSLIM. When the slab detaches and sinks into the mantle, magnitudes of  $F_{\text{SP}}$  increase rapidly to ca.  $40 \text{ TN m}^{-1}$  in SLIM200, ca.  $42 \text{ TN m}^{-1}$  in SLIM300 and

again ca.  $40 \text{ TN m}^{-1}$  in NOSLIM. This rapid increase of  $F_{\text{SP}}$  occurs ca. 4, 13 and 21 Myr after the slab has transected  $y = -410 \text{ km}$  in SLIM200, SLIM300 and NOSLIM, respectively. The depths of slab detachment also vary from  $y \approx -200 \text{ km}$  in NOSLIM,  $y \approx -150 \text{ km}$  in SLIM300 to  $y \approx -30 \text{ km}$  in SLIM200 (**Figure 9**). In SLIM100 the magnitude of  $F_{\text{SP}}$  increases slowly to ca.  $30 \text{ TN m}^{-1}$  until ca. 156 Myr. At this stage, drip-off of the lithosphere occurs in this model (**Figure 6D**).

## 4 DISCUSSION

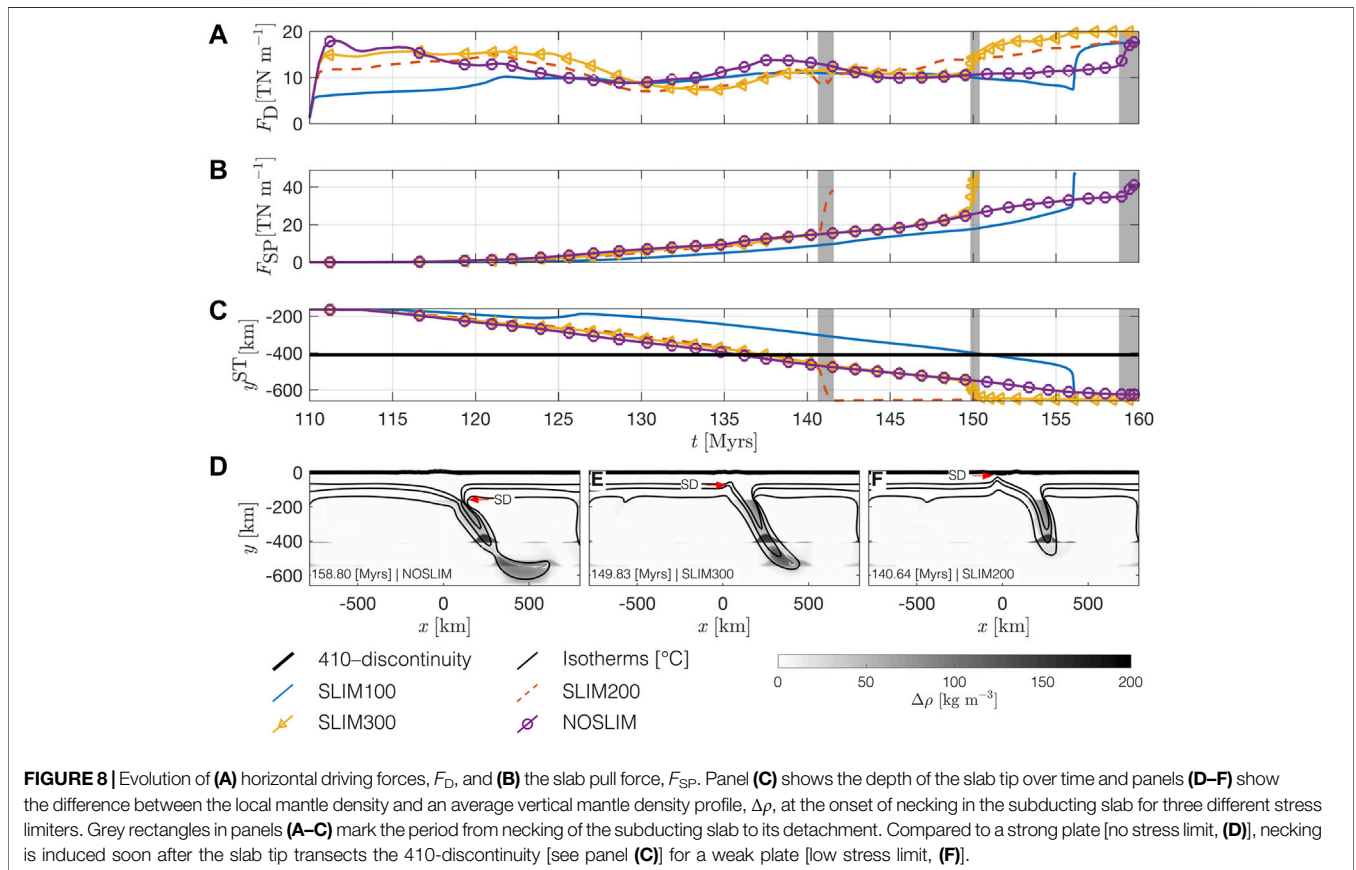
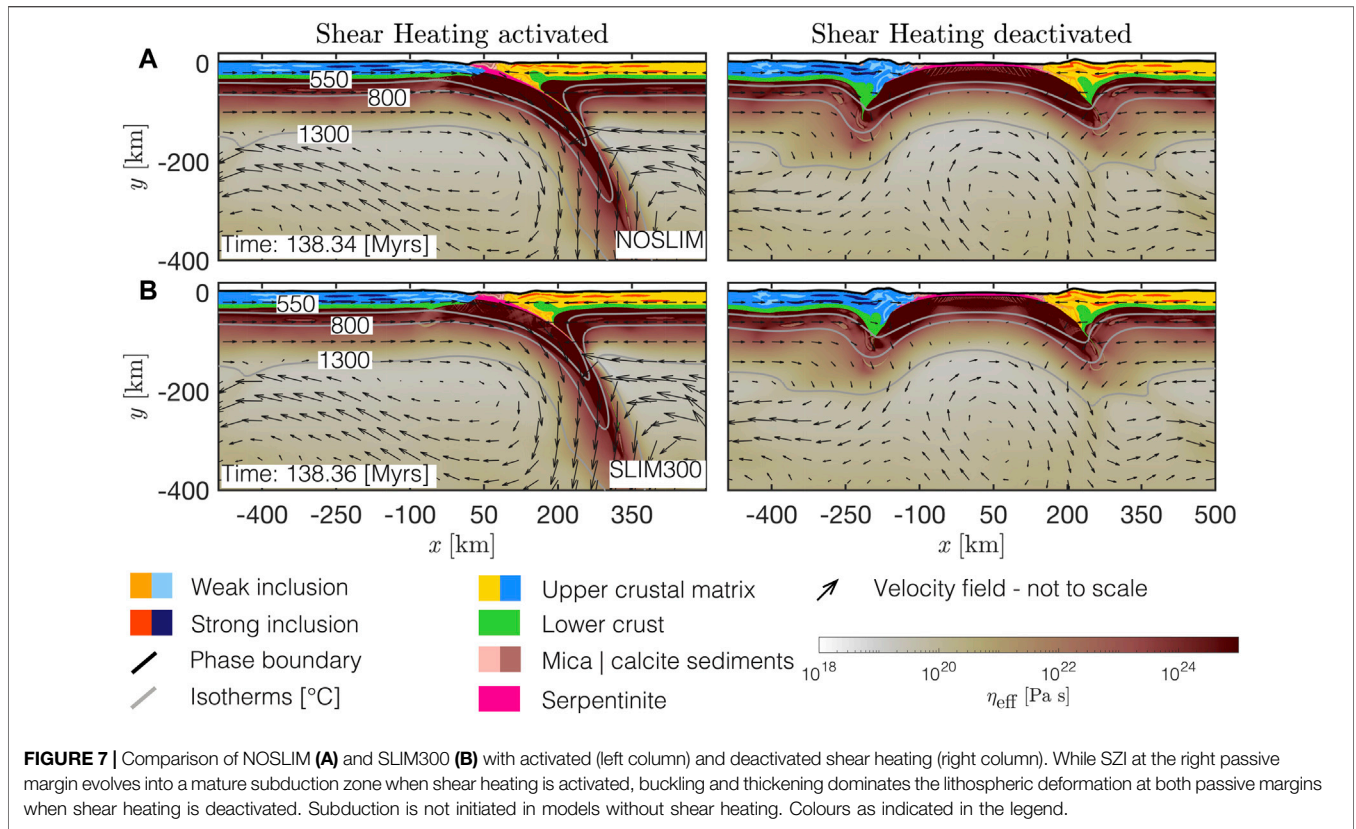
### 4.1 Subduction Initiation via Thermal Softening

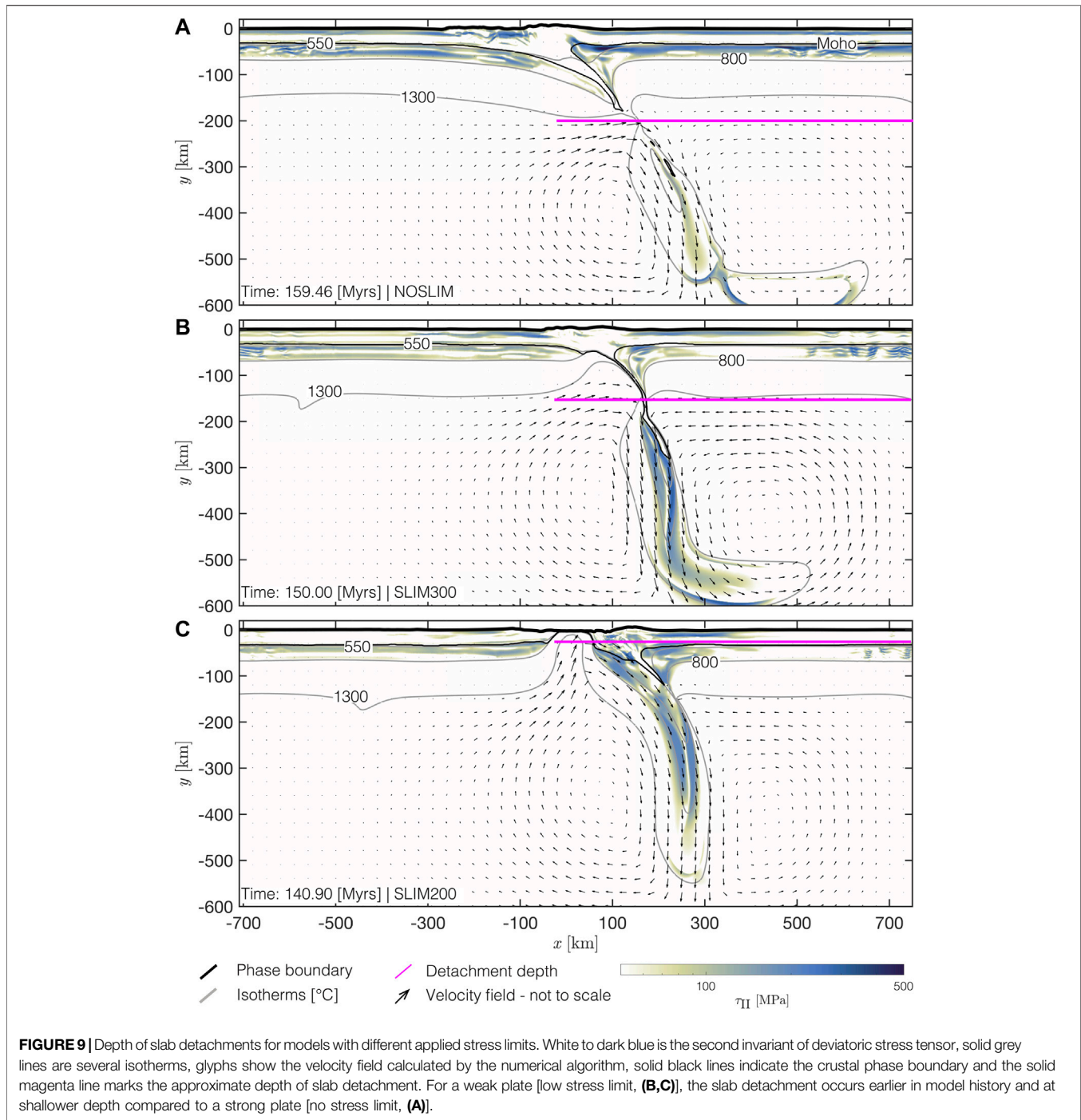
In combination with temperature-dependent rheologies, shear heating is potentially a feasible mechanism to form a shear zone transecting the lithosphere (Yuen et al., 1978; Thielmann and Kaus, 2012; Jaquet and Schmalholz, 2018) and initiate subduction at a hyperextended continental



margin (Candiotti et al., 2021). Kiss et al. (2019) derived an equation to predict the maximum temperature rise inside a shear zone,  $T_{SH}$  (Eq. 22 in Kiss et al., 2019), that is formed *via* shear heating. This prediction relies only on material parameters and the applied absolute horizontal velocity difference, and has already been applied to SZI at homogeneous hyperextended continental margins (Kiss et al., 2020). According to their prediction, a temperature rise by 50°C is sufficient for spontaneous shear localisation *via* shear heating and the associated thermal softening. In our models, the dissipation created by the conversion of mechanical work into heat is ca.  $10^{-5} \text{ W m}^{-3}$ . Consequently, the temperature increases by 50–90°C in models SLIM200, SLIM300 and NOSLIM. Due to thermal diffusion such a moderate temperature increase is likely not detectable in natural shear zones having a thickness in the order of a few kilometers (e.g., Kiss et al., 2019). The temperature inside the evolving shear zone can be predicted by the equation of Kiss et al. (2019) (deflection of grey solid lines in Figures 4A,B). Therefore, shear heating is efficient for stresses inside the lithospheric mantle

that are as low as ca. 200 MPa in our models. This stress magnitude represents the maximum stress during the onset of the formation of a shear zone and stresses are decreasing during progressive shear zone formation (Kiss et al., 2019). This observation is crucial as shear heating is often criticized for requiring too high stresses to be an efficient mechanism for ductile shear zone localization (e.g., Platt, 2015). Furthermore, Kiss et al. (2019) reported that shear heating is already efficient for stresses as low as 200 MPa. The predicted temperature inside the shear zone forming in SLIM200 is still accurate, although the deformation inside and around the shear zone is mainly occurring in the brittle-plastic field due to the low stress limit (Figure 5C). Although the generated dissipation is relatively lower compared to higher stress limiters, the temperature increase in SLIM200 and SLIM300 are comparable (compare isotherms in Figures 4B,C). The estimated temperature increase of ca. 50°C in SLIM200 is the limit for shear heating causing spontaneous shear localisation predicted by Kiss et al. (2019). This indicates that likely ductile and brittle-plastic processes are equally



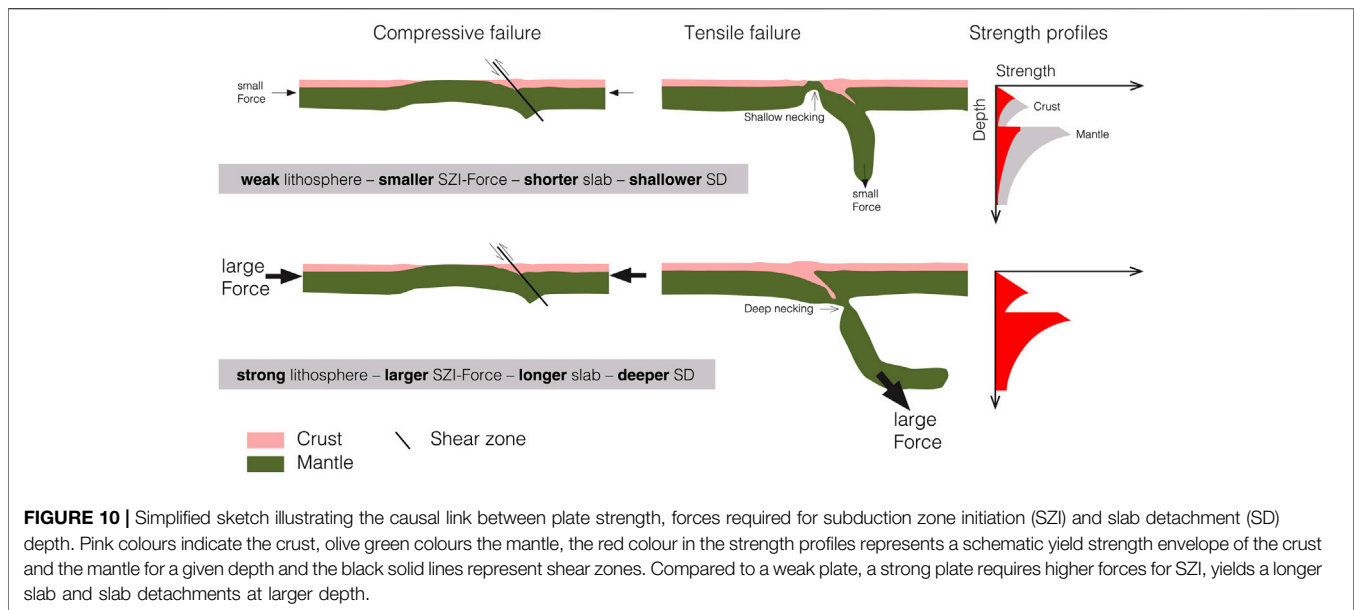


important for shear zone localization in model SLIM200. In case stresses are lower than 200 MPa, brittle-plastic processes dominate the deformation inside the lithospheric mantle and shear heating is likely inefficient (flat grey isotherm in **Figure 5D**). Thielmann and Kaus (2012), Jaquet and Schmalholz (2018) and Kiss et al. (2020) already showed that in absence of other softening mechanisms, thermal softening is required for convergent plate boundary formation and successful SZI in lithospheric-scale geodynamic models. We here confirm these results. In the models we present,

thermal softening is indeed the responsible mechanism that causes SZI (see **Figure 7**).

#### 4.2 Horizontal and Slab-Pull Forces

We report a minimum magnitude of ca. 14–15 TN m<sup>-1</sup> for horizontal plate driving forces required for SZI *via* shear heating (SLIM200 and SLIM300, **Figure 8A**). While a magnitude of ca. 30–37 TN m<sup>-1</sup> for plate driving forces was required to initiate subduction at a homogeneous continental



margin in the models of Kiss et al. (2020) and Auzemery et al. (2021), we here report a maximum value of ca.  $18 \text{ TN m}^{-1}$  for a continental margin that includes elliptical mechanical heterogeneities. Subduction initiation at ca.  $10 \text{ TN m}^{-1}$  is observed in SLIM100. However, subduction initiation in this model is controlled by brittle-plastic deformation rather than by shear heating. In our model SLIM100, the lithospheric deformation style changes from a subduction (Figure 6C) into a delamination, or drip-off, style with ongoing convergence (Figure 6D). Such drip-off deformation behaviour is consistent with earlier studies on subduction initiation within mechanically weak lithospheric plates (e.g., Thielmann and Kaus, 2012). We therefore propose that the minimum driving force magnitude predicted by SLIM200 and SLIM300 of  $14\text{--}15 \text{ TN m}^{-1}$  are likely more meaningful estimates for SZI at natural geodynamic settings than the magnitude predicted by SLIM100. This magnitude could likely be further reduced by modulating, for example, the olivine dislocation and Peierls flow law parameters.

The density difference between the slab and the surrounding mantle due to the uplift of the olivine-wadsleyite phase transition (at  $y = -410 \text{ km}$ ) in our models is between ca.  $150\text{--}200 \text{ kg m}^{-3}$ . This petrological-thermomechanically coupled density prediction is slightly lower but overall in good agreement with previous estimates ( $275 \text{ kg m}^{-3}$ , Turcotte and Schubert, 2014). This increase in density causes an increase in slab pull force magnitude of ca.  $16 \text{ TN m}^{-1}$  (Turcotte and Schubert, 2014). Although this estimate is based on buoyancy only and does not consider shear forces along the subducting slab, it is meaningful as these shear forces already act on the slab before the phase change. Our model SLIM200 confirms this estimate. A sharp increase in slab pull force occurs when a magnitude of ca.  $17 \text{ TN m}^{-1}$  is reached at ca. 141 Myr (Figure 8B). In SLIM200, SD begins immediately after the slab has transited a depth of

410 km (Figures 8C,F). This observation indicates that slabs must at least be strong enough to support the additional pull force induced by the phase transition in order to penetrate further into the mantle without detaching immediately after the olivine-wadsleyite phase transition occurs within the slab.

In our models we observe the following correlation between the slab strength and the timing of slab detachment: The weaker the slab, the earlier it detaches after transiting the olivine-wadsleyite phase transition. We further observe a correlation between the strength of the slab and the depth of the detachment: weak slabs detach already in the horizontal region of the subducting plate, whereas strong slabs detach in ca. 100–200 km depth (Figure 10). In all models, the slab detaches within ca. 1 Myr from the onset of necking. These observations are consistent with earlier studies of slab detachment (e.g., Andrews and Billen, 2009; Baumann et al., 2010; Duretz et al., 2011a; Schmalholz, 2011; van Hunen and Allen, 2011; Thielmann and Schmalholz, 2020). The estimates for slab pull forces we report here are between ca. 18 and  $35 \text{ TN m}^{-1}$ . These magnitudes are lower than previous calculations (e.g., Forsyth and Uyeda, 1975). However, these magnitudes only consider forces arising from buoyancy contrasts between the subducting slab and the surrounding mantle and do not include viscous tractions along the slab. Such tractions reduce the effective slab pull force (e.g., Schellart, 2004).

### 4.3 Implications for Natural Subduction Zone Initiation and Slab Detachment

Natural orogens like the Variscides, the Pyrenees or the European Alps may have resulted from the closure of narrow oceanic basins (e.g., Chenin et al., 2019). These immature extensional systems are characterized by insignificant production of new, mature oceanic lithosphere and subduction of these embryonic oceans

produce insignificant amounts of volcanic arc-basalts (e.g., McCarthy et al., 2020). In absence of a significant active mid-ocean ridge, such embryonic basin-margin system is likely more laterally homogeneous (due to lack of a ridge) compared to an ocean basin including a significant spreading ridge. Consequently, embryonic ocean basins likely lack significant lateral variation in temperature and, therefore, strength. Hence, the closure of such basins from SZI to SD may be considered as, respectively, natural compressive and tensile failure tests of the lithosphere. The models we present have significant implications for these natural systems. For example, subduction in the Western Alpine-Tethys presumably initiated below the hyperextended continental margin of the Adriatic plate at ca. 85 Ma (e.g., Manzotti et al., 2014) and lead to closure of the embryonic Piemonte-Liguria ocean (e.g., McCarthy et al., 2020). Our models predict that, compared to a weak subducting lithosphere, a strong lithosphere requires higher forces to fail under compression and yield SZI and plate boundary formation. However, under tension, which develops due to increasing pull forces induced by the subducting slab, the same strong lithosphere may be able to hold a continuous subducting slab down to 660 km depth over more than 20 Myr after basin closure. In contrast, a weak lithosphere fails immediately under tension and exhibits shallow SD early after closure of the embryonic ocean basin. This result may help explaining the strong east-west variability of slab geometries observed in tomographic images from the present-day European Alps (e.g., Lippitsch et al., 2003; Hua et al., 2017; Kästle et al., 2019).

Our models NOSLIM and SLIM300 (Figures 9A,B) suggest that the embryonic Piemonte-Liguria ocean might have been weaker in the east compared to the centre which lead to early and shallow slab break-off in the eastern Alps (slab gap, Lippitsch et al., 2003) whereas the slab remained more or less intact in the central region (Zhao et al., 2016). The resulting asthenospheric window in the slab (see glyphs in Figure 9B) below the eastern Alps might have induced a heat pulse in the crustal units (e.g., Davies and von Blanckenburg, 1995). For example, in simulation SLIM300 the 1,300°C isotherm is uplifted towards shallower depth in the region of SD (Figure 9B). The 1,300°C isotherm is uplifted to approximately the same depth as that of the horizontal 800°C isotherm to the left and right side of the region with SD. Therefore, the temperature can be locally increased by ca. 500°C with respect to temperatures in an undeformed lithosphere. Such local temperature increase due to SD might contribute to magmatism associated with the Bergell intrusion, which has been explained by SD (e.g., Davies and von Blanckenburg, 1995). Certainly, the Alps have a distinct 3D architecture and our models are only two-dimensional. Previous three-dimensional modelling studies have studied the impact of along-strike variations on the process of slab detachment (van Hunen and Allen, 2011; von Tscharnier et al., 2014; Duretz et al., 2014). Because of their two-dimensional nature, our models do not capture along-strike propagation of slab detachment. Nevertheless, they successfully account for the physics of necking which is the

underlying physical process governing slab detachment (e.g., Schmalholz, 2011; Duretz et al., 2012). Moreover, lateral propagation of slab detachment is triggered by asymmetries in the lateral structure of collision zones (van Hunen and Allen, 2011), which remain difficult to constrain through the course of the Alpine history. We hence suggest that our models remain applicable, at first order, to the study of slab detachment in the Alps.

Slab detachment is a short-lived process and we just mention also briefly two regions in which SD is presumably occurring at present day. In the Vrancea area (e.g., Wenzel et al., 1998) a nearly vertically hanging slab which is still attached to the overlying plate induces earthquakes at an intermediate depth between 70 and 180 km. However, the maximum depth of the slab might be much deeper (Sperner et al., 2001; Ferrand and Manea, 2021). Also, recent seismic data from the Hindu Kush indicates a potential onset of slab detachment or delamination at depths of ca. 200 km (e.g., Kufner et al., 2021). Such detachment depths are well predicted by our models (Figures 8D-F).

#### 4.4 Constraining the Lithospheric Strength With Numerical Models

Three-dimensional numerical models of global mantle convection have been used to constrain the effective strength of the lithosphere. Mallard et al. (2016), for example, applied a constant von-Mises stress limiter function in their models (similar to this study) and showed that stress magnitudes between 150 and 200 MPa in the lithosphere result in the most realistic plate-like behaviour. The model results of SLIM200 confirm the results reported by Mallard et al. (2016). However, our models predict plate-like behaviour also for stresses higher than 200 MPa in the lithosphere (see for example model NOSLIM), likely because of the higher numerical resolution. In our models, high stresses in the lithosphere are limited to a 10–25 km thin, load-bearing layer (see f.e. Figures 3E-H). Such thin layers cannot be resolved numerically in most global mantle convection models. In comparison, dividing, for example,  $F_D = 18 \text{ TN m}^{-1}$ , which was necessary to overcome the plate strength in NOSLIM and initiate subduction, by a ca. 50 km thick lithosphere yields an average deviatoric stress of ca. 180 MPa which agrees with the equivalent von-Mises shear stress between 150 and 200 MPa of Mallard et al. (2016), which is required to generate a plate size-frequency distribution observed for Earth. Therefore, the magnitude of the horizontal driving forces in our numerical simulations agree with horizontal forces predicted by recent global mantle convection models.

Because of the high numerical resolution, our models can test first the resistance of plates to failure under variable applied compressive stresses (during SZI) and subsequently under variable tensile stresses (during SD). Therefore, models as presented here may represent a complementary method to classical laboratory experiments, inversion from geophysical data and global mantle convection models and help to better constrain the effective strength of the lithosphere.

## 5 CONCLUSION

We presented 2D petrological-thermomechanical models for the convergence of embryonic ocean basins bounded by passive margins to quantify the minimum horizontal force required for subduction zone initiation (SZI) at passive margins. Although we also include an initially horizontal weak serpentinite layer in the ocean basin, our results show that this layer has no impact on SZI. In our models, plate boundary formation and SZI is controlled by thermal softening caused by shear heating. Simulations in which shear heating only is deactivated do not show SZI which clearly shows that shear heating and associated thermal softening controls SZI in our models. A temperature increase due to shear heating inside a shear zone of only ca. 50°C is sufficient for successful SZI. The minimum horizontal force (per unit length) required for such SZI is between 14 and 15 TN m<sup>-1</sup>. Dividing 15 TN m<sup>-1</sup> by a lithosphere thickness of 50 km (representing the region with significant strength) yields a shear stress of 150 MPa. Such shear stress magnitude is consistent with average lithospheric yield stress estimates based on 3D spherical models of mantle convection in order to self-consistently produce the plate size–frequency distribution observed for Earth. Consequently, we conclude that 1) shear heating and associated thermal softening is a feasible mechanism for horizontally-forced SZI at passive margins and 2) the required horizontal force magnitudes for such SZI are realistic and in agreement with independent estimates from global mantle convection models.

The convergence and closure of ocean basins bounded by passive margins involves two geodynamic processes that are controlled by the effective strength of the lithosphere: SZI, controlled by the compressive strength of the lithosphere, and subsequent slab detachment (SD), controlled by the tensile strength. Therefore, the compressive force magnitude required to “break” the lithosphere during horizontally forced SZI is linked to the tensile force required to “break” the lithosphere during SD. Our results show that the smaller the horizontal force required for SZI, the earlier and shallower SD occurs during basin closure and the shorter is the length of the slab. We presented one simulation with a stress limit in the lithosphere of 200 MPa (corresponding to a horizontal force during SZI of 14 TN m<sup>-1</sup>) which showed a

successful SZI. However, the lithosphere was so weak that the subducting lithosphere detached already in the horizontal, non-subducted region of the lithospheric plate shortly before basin closure. Such horizontal slab detachment is most likely unrealistic for most natural settings such as for the closure of the Piemonte-Liguria ocean during Alpine orogeny. In the Alps, the slab geometries are still contentious with some studies proposing slab detachment linked to the Europe-Adria collision some 30 Myrs ago while other studies argue that there was no slab detachment. Our results imply that if there was no slab detachment since the Europe-Asia collision, as suggested by some studies, then the corresponding slab must have a large effective strength to prohibit SD.

We propose that the closure of ocean basins involving both SZI and SD can be considered as a natural “experiment” that tests both the effective compressive and tensile strength of the lithosphere. Consequently, we propose that numerical studies on horizontally-forced SZI also should test whether their models can generate a significant slab which can support realistic slab pull forces in order to avoid that SZI is studied for an unrealistically weak lithosphere.

## DATA AVAILABILITY STATEMENT

The raw data supporting the conclusion of this article will be made available by the authors, without undue reservation.

## AUTHOR CONTRIBUTIONS

LC conducted the numerical simulations, interpreted the results and wrote the manuscript. TD developed the applied numerical algorithm, helped interpreting the results and writing the manuscript. SS conceptualized and supervised the study, helped interpreting the results and writing the manuscript.

## FUNDING

This study was supported by SNSF grant No. 200020 163169.

## REFERENCES

- Aharonov, E., and Scholz, C. H. (2018). A Physics-Based Rock Friction Constitutive Law: Steady State Friction. *J. Geophys. Res. Solid Earth* 123, 1591–1614. doi:10.1002/2016jb013829
- Andrews, E. R., and Billen, M. I. (2009). Rheologic Controls on the Dynamics of Slab Detachment. *Tectonophysics* 464, 60–69. doi:10.1016/j.tecto.2007.09.004
- Auzemery, A., Willingshofer, E., Yamato, P., Duretz, T., and Beekman, F. (2021). Kinematic Boundary Conditions Favouring Subduction Initiation at Passive Margins over Subduction at Mid-oceanic Ridges. *Front. Earth Sci.* 9. doi:10.3389/feart.2021.765893
- Auzemery, A., Willingshofer, E., Yamato, P., Duretz, T., and Sokoutis, D. (2020). Strain Localization Mechanisms for Subduction Initiation at Passive Margins. *Glob. Planet. Change* 195, 103323. doi:10.1016/j.gloplacha.2020.103323
- Baumann, C., Gerya, T. V., and Connolly, J. A. D. (2010). Numerical Modelling of Spontaneous Slab Breakoff Dynamics during continental Collision. *Geol. Soc. Lond. Spec. Publications* 332, 99–114. doi:10.1144/sp332.7
- Baumann, T. S., Kaus, B. J. P., and Popov, A. A. (2014). Constraining Effective Rheology through Parallel Joint Geodynamic Inversion. *Tectonophysics* 631, 197–211. doi:10.1016/j.tecto.2014.04.037
- Bercovici, D., and Ricard, Y. (2012). Mechanisms for the Generation of Plate Tectonics by Two-phase Grain-Damage and Pinning. *Phys. Earth Planet. Interiors* 202–203, 27–55. doi:10.1016/j.pepi.2012.05.003
- Burov, E. B., and Watts, A. B. (2006). The Long-Term Strength of continental Lithosphere: “jelly sandwich” or “crème brûlée”? *GSA today* 16, 4. doi:10.1130/1052-5173(2006)016<4:tltsoc>2.0.co;2
- Candiotti, L. G., Duretz, T., Moulas, E., and Schmalholz, S. M. (2021). Buoyancy versus Shear Forces in Building Orogenic Wedges. *Solid Earth* 12, 1749–1775. doi:10.5194/se-12-1749-2021
- Candiotti, L. G., Schmalholz, S. M., and Duretz, T. (2020). Impact of Upper Mantle Convection on Lithosphere Hyperextension and Subsequent Horizontally

- Forced Subduction Initiation. *Solid Earth* 11, 2327–2357. doi:10.5194/se-11-2327-2020
- Chenin, P., Manatschal, G., Picazo, S., Müntener, O., Karner, G., Johnson, C., et al. (2017). Influence of the Architecture of Magma-Poor Hyperextended Rifted Margins on Orogens Produced by the Closure of Narrow versus Wide Oceans. *Geosphere* 13, 559–576. doi:10.1130/ges01363.1
- Chenin, P., Picazo, S., Jammes, S., Manatschal, G., Müntener, O., and Karner, G. (2019). Potential Role of Lithospheric Mantle Composition in the Wilson Cycle: a north Atlantic Perspective. *Geol. Soc. Lond. Spec. Publications* 470, 157–172. doi:10.1144/sp470.10
- Cloetingh, S., Wortel, R., and Vlaar, N. J. (1989). “On the Initiation of Subduction Zones,” in *Subduction Zones Part II* (Berlin, Germany: Springer), 7–25. doi:10.1007/978-3-0348-9140-0\_2
- Connolly, J. A. D. (2005). Computation of Phase Equilibria by Linear Programming: a Tool for Geodynamic Modeling and its Application to Subduction Zone Decarbonation. *Earth Planet. Sci. Lett.* 236, 524–541. doi:10.1016/j.epsl.2005.04.033
- Connolly, J. (2009). The Geodynamic Equation of State: what and How. *Geochem. Geophys. Geosystems* 10. doi:10.1029/2009gc002540
- Cramer, F., Magni, V., Domeier, M., Shephard, G. E., Chotalia, K., Cooper, G., et al. (2020). A Transdisciplinary and Community-Driven Database to Unravel Subduction Zone Initiation. *Nat. Commun.* 11, 3750. doi:10.1038/s41467-020-17522-9
- Dannowski, A., Kopp, H., Grevemeyer, I., Lange, D., Thorwart, M., Bialas, J., et al. (2020). Seismic Evidence for Failed Rifting in the Ligurian basin, Western alpine Domain. *Solid Earth* 11, 873–887. doi:10.5194/se-11-873-2020
- Demouchy, S., Tommasi, A., Boffa Ballaran, T., and Cordier, P. (2013). Low Strength of Earth’s Uppermost Mantle Inferred from Tri-axial Deformation Experiments on Dry Olivine Crystals. *Phys. Earth Planet. Interiors* 220, 37–49. doi:10.1016/j.pepi.2013.04.008
- Duretz, T., Gerya, T. V., and May, D. A. (2011a). Numerical Modelling of Spontaneous Slab Breakoff and Subsequent Topographic Response. *Tectonophysics* 502, 244–256. doi:10.1016/j.tecto.2010.05.024
- Duretz, T., Gerya, T. V., and Spakman, W. (2014). Slab Detachment in Laterally Varying Subduction Zones: 3-d Numerical Modeling. *Geophys. Res. Lett.* 41, 1951–1956. doi:10.1002/2014GL059472
- Duretz, T., May, D. A., Gerya, T., and Tackley, P. (2011b). Discretization Errors and Free Surface Stabilization in the Finite Difference and Marker-In-Cell Method for Applied Geodynamics: A Numerical Study. *Geochem. Geophys. Geosystems* 12. doi:10.1029/2011gc003567
- Duretz, T., May, D. A., and Yamato, P. (2016). A Free Surface Capturing Discretization for the Staggered Grid Finite Difference Scheme. *Geophys. J. Int.* 204, 1518–1530. doi:10.1093/gji/ggv526
- Duretz, T., Schmalholz, S., and Gerya, T. (2012). Dynamics of Slab Detachment. *Geochem. Geophys. Geosystems* 13. doi:10.1029/2011gc004024
- Dymkova, D., and Gerya, T. (2013). Porous Fluid Flow Enables Oceanic Subduction Initiation on Earth. *Geophys. Res. Lett.* 40, 5671–5676. doi:10.1002/2013gl057798
- Ferrand, T. P., and Manea, E. F. (2021). Dehydration-induced Earthquakes Identified in a Subducted Oceanic Slab beneath Vrancea, Romania. *Sci. Rep.* 11, 10315–10319. doi:10.1038/s41598-021-89601-w
- Forsyth, D., and Uyeda, S. (1975). On the Relative Importance of the Driving Forces of Plate Motion. *Geophys. J. Int.* 43, 163–200. doi:10.1111/j.1365-246x.1975.tb00631.x
- Furstoss, J., Petit, C., Tommasi, A., Ganino, C., Muñoz, D. P., and Bernacki, M. (2021). On the Role of Solute Drag in Reconciling Laboratory and Natural Constraints on Olivine Grain Growth Kinetics. *Geophys. J. Int.* 224, 1360–1370.
- Gerya, T. V., and Yuen, D. A. (2003). Characteristics-based Marker-In-Cell Method with Conservative Finite-Differences Schemes for Modeling Geological Flows with Strongly Variable Transport Properties. *Phys. Earth Planet. Interiors* 140, 293–318. doi:10.1016/j.pepi.2003.09.006
- Goetze, C., and Evans, B. (1979). Stress and Temperature in the Bending Lithosphere as Constrained by Experimental Rock Mechanics. *Geophys. J. Int.* 59, 463–478. doi:10.1111/j.1365-246x.1979.tb02567.x
- Handy, M. R., Schmid, S., Bousquet, R., Kissling, E., and Bernoulli, D. (2010). Reconciling Plate-Tectonic Reconstructions of Alpine Tethys with the Geological-Geophysical Record of Spreading and Subduction in the Alps. *Earth-Science Rev.* 102, 121–158. doi:10.1016/j.earscirev.2010.06.002
- Hansen, F., and Carter, N. (1983). “Semibrittle Creep of Dry and Wet Westerly Granite at 1000 MPa,” in *The 24th US Symposium on Rock Mechanics (USRMS)*.
- Hansen, L. N., Kumamoto, K. M., Thom, C. A., Wallis, D., Durham, W. B., Goldsby, D. L., et al. (2019). Low-Temperature Plasticity in Olivine: Grain Size, Strain Hardening, and the Strength of the Lithosphere. *J. Geophys. Res. Solid Earth* 124, 5427–5449. doi:10.1029/2018jb016736
- Hilalret, N., Reynard, B., Wang, Y., Daniel, I., Merkel, S., Nishiyama, N., et al. (2007). High-pressure Creep of Serpentine, Interseismic Deformation, and Initiation of Subduction. *Science* 318, 1910–1913. doi:10.1126/science.1148494
- Hirth, G., and Kohlstedt, D. (2003). Rheology of the Upper Mantle and the Mantle Wedge: A View from the Experimentalists. *Geophys. Monograph-American Geophys. Union* 138, 83–105. doi:10.1029/138gm06
- Hua, Y., Zhao, D., and Xu, Y. (2017). P Wave Anisotropic Tomography of the Alps. *J. Geophys. Res. Solid Earth* 122, 4509–4528. doi:10.1002/2016jb013831
- Huw Davies, J., and von Blanckenburg, F. (1995). Slab Breakoff: a Model of Lithosphere Detachment and its Test in the Magmatism and Deformation of Collisional Orogens. *Earth Planet. Sci. Lett.* 129, 85–102. doi:10.1016/0012-821x(94)00237-s
- Idrissi, H., Bollinger, C., Bovioli, F., Schryvers, D., and Cordier, P. (2016). Low-temperature Plasticity of Olivine Revisited with *In Situ* Tem Nanomechanical Testing. *Sci. Adv.* 2, e1501671. doi:10.1126/sciadv.1501671
- Jaquet, Y., and Schmalholz, S. M. (2018). Spontaneous Ductile Crustal Shear Zone Formation by thermal Softening and Related Stress, Temperature and Strain Rate Evolution. *Tectonophysics* 746, 384–397. doi:10.1016/j.tecto.2017.01.012
- Kameyama, M., Yuen, D. A., and Karato, S.-I. (1999). Thermal-mechanical Effects of Low-Temperature Plasticity (The Peierls Mechanism) on the Deformation of a Viscoelastic Shear Zone. *Earth Planet. Sci. Lett.* 168, 159–172. doi:10.1016/s0012-821x(99)00040-0
- Kästle, E. D., Rosenberg, C., Boschi, L., Bellahsen, N., Meier, T., and El-Sharkawy, A. (2019). Slab Break-Offs in the alpine Subduction Zone. *Solid Earth Discuss.* 2019, 1–19.
- Kiss, D., Candioti, L. G., Duretz, T., and Schmalholz, S. M. (2020). Thermal Softening Induced Subduction Initiation at a Passive Margin. *Geophys. J. Int.* 220, 2068–2073. doi:10.1093/gji/ggz572
- Kiss, D., Podladchikov, Y., Duretz, T., and Schmalholz, S. M. (2019). Spontaneous Generation of Ductile Shear Zones by thermal Softening: Localization Criterion, 1D to 3D Modelling and Application to the Lithosphere. *Earth Planet. Sci. Lett.* 519, 284–296. doi:10.1016/j.epsl.2019.05.026
- Kronenberg, A. K., Kirby, S. H., and Pinkston, J. (1990). Basal Slip and Mechanical Anisotropy of Biotite. *J. Geophys. Res.* 95, 19257–19278. doi:10.1029/jb095ib12p19257
- Kufner, S. K., Kakar, N., Bezada, M., Bloch, W., Metzger, S., Yuan, X., et al. (2021). The Hindu Kush Slab Break-Off as Revealed by Deep Structure and Crustal Deformation. *Nat. Commun.* 12, 1685. doi:10.1038/s41467-021-21760-w
- Lallemand, S., and Arcay, D. (2021). Subduction Initiation from the Earliest Stages to Self-Sustained Subduction: Insights from the Analysis of 70 Cenozoic Sites. *Earth-Science Rev.* 221, 103779. doi:10.1016/j.earscirev.2021.103779
- Le Breton, E., Brune, S., Ustaszewski, K., Zahirovic, S., Seton, M., and Müller, R. D. (2021). Kinematics and Extent of the Piemont-Liguria Basin - Implications for Subduction Processes in the Alps. *Solid Earth* 12, 885–913. doi:10.5194/se-12-885-2021
- Leloup, P. H., Ricard, Y., Battaglia, J., and Lacassin, R. (1999). Shear Heating in continental Strike-Slip Shear Zones: model and Field Examples. *Geophys. J. Int.* 136, 19–40. doi:10.1046/j.1365-246x.1999.00683.x
- Lippitsch, R., Kissling, E., and Ansgor, J. (2003). Upper Mantle Structure beneath the alpine Orogen from High-Resolution Teleseismic Tomography. *J. Geophys. Res. Solid Earth* 108. doi:10.1029/2002jb002016
- Mackwell, S. J., Zimmerman, M. E., and Kohlstedt, D. L. (1998). High-temperature Deformation of Dry Diabase with Application to Tectonics on Venus. *J. Geophys. Res.* 103, 975–984. doi:10.1029/97jb02671
- Malatesta, C., Gerya, T., Crispini, L., Federico, L., and Capponi, G. (2013). Oblique Subduction Modelling Indicates Along-Trench Tectonic Transport of Sediments. *Nat. Commun.* 4, 2456–6. doi:10.1038/ncomms3456

- Mallard, C., Coltice, N., Seton, M., Müller, R. D., and Tackley, P. J. (2016). Subduction Controls the Distribution and Fragmentation of Earth's Tectonic Plates. *Nature* 535, 140–143. doi:10.1038/nature17992
- Manzotti, P., Ballèvre, M., Zucali, M., Robyr, M., and Engi, M. (2014). The Tectonometamorphic Evolution of the Sesia-Dent Blanche Nappes (Internal Western Alps): Review and Synthesis. *Swiss J. Geosci.* 107, 309–336. doi:10.1007/s00015-014-0172-x
- McCarthy, A., Tugend, J., Mohn, G., Candiotti, L., Chelle-Michou, C., Arculus, R., et al. (2020). A Case of Ampferer-type Subduction and Consequences for the Alps and the Pyrenees. *Am. J. Sci.* 320, 313–372. doi:10.2475/04.2020.01
- McKenzie, D. P. (1977). The Initiation of Trenches: a Finite Amplitude Instability. *Isl. arcs, deep sea trenches back-arc basins* 1, 57–61. doi:10.1029/me001p0057
- Montési, L. G. (2013). Fabric Development as the Key for Forming Ductile Shear Zones and Enabling Plate Tectonics. *J. Struct. Geology*. 50, 254–266.
- Mueller, S., and Phillips, R. J. (1991). On the Initiation of Subduction. *J. Geophys. Res.* 96, 651–665. doi:10.1029/90jb02237
- Müller, R. D., Sdrolias, M., Gaina, C., and Roest, W. R. (2008). Age, Spreading Rates, and Spreading Asymmetry of the World's Ocean Crust. *Geochem. Geophys. Geosystems* 9.
- Mulyukova, E., and Bercovici, D. (2018). Collapse of Passive Margins by Lithospheric Damage and Plunging Grain Size. *Earth Planet. Sci. Lett.* 484, 341–352. doi:10.1016/j.epsl.2017.12.022
- Platt, J. P. (2015). Influence of Shear Heating on Microstructurally Defined Plate Boundary Shear Zones. *J. Struct. Geology*. 79, 80–89. doi:10.1016/j.jsg.2015.07.009
- Ranalli, G. (1995). *Rheology of the Earth*. Berlin, Germany: Springer Science & Business Media.
- Regenauer-Lieb, K., Yuen, D. A., and Branlund, J. (2001). The Initiation of Subduction: Criticality by Addition of Water? *science* 294, 578–580. doi:10.1126/science.1063891
- Regenauer-Lieb, K., and Yuen, D. A. (1998). Rapid Conversion of Elastic Energy into Plastic Shear Heating during Incipient Necking of the Lithosphere. *Geophys. Res. Lett.* 25, 2737–2740. doi:10.1029/98gl02056
- Rybacki, E., and Dresen, G. (2004). Deformation Mechanism Maps for Feldspar Rocks. *Tectonophysics* 382, 173–187. doi:10.1016/j.tecto.2004.01.006
- Schellart, W. (2004). Quantifying the Net Slab Pull Force as a Driving Mechanism for Plate Tectonics. *Geophys. Res. Lett.* 31. doi:10.1029/2004gl019528
- Schmalholz, S. M. (2011). A Simple Analytical Solution for Slab Detachment. *Earth Planet. Sci. Lett.* 304, 45–54. doi:10.1016/j.epsl.2011.01.011
- Schmalholz, S. M., Duretz, T., Hetényi, G., and Medvedev, S. (2019). Distribution and Magnitude of Stress Due to Lateral Variation of Gravitational Potential Energy between Indian lowland and Tibetan Plateau. *Geophys. J. Int.* 216, 1313–1333. doi:10.1093/gji/ggy463
- Schmalholz, S. M., and Fletcher, R. C. (2011). The Exponential Flow Law Applied to Necking and Folding of a Ductile Layer. *Geophys. J. Int.* 184, 83–89. doi:10.1111/j.1365-246x.2010.04846.x
- Schmalholz, S. M., Medvedev, S., Lechmann, S. M., and Podladchikov, Y. (2014). Relationship between Tectonic Overpressure, Deviatoric Stress, Driving Force, Isostasy and Gravitational Potential Energy. *Geophys. J. Int.* 197, 680–696. doi:10.1093/gji/ggu040
- Schmid, S. M., Boland, J. N., and Paterson, M. S. (1977). Superplastic Flow in Finegrained limestone. *Tectonophysics* 43, 257–291. doi:10.1016/0040-1951(77)90120-2
- Schmid, S. M., Kissling, E., Diehl, T., van Hinsbergen, D. J. J., and Molli, G. (2017). Ivrea Mantle Wedge, Arc of the Western Alps, and Kinematic Evolution of the Alps-Apennines Orogenic System. *Swiss J. Geosci.* 110, 581–612. doi:10.1007/s00015-016-0237-0
- Shuck, B., Gulick, S. P. S., Van Avendonk, H. J. A., Gurnis, M., Sutherland, R., Stock, J., et al. (2022). Stress Transition from Horizontal to Vertical Forces during Subduction Initiation. *Nat. Geosci.* 15, 149–155. doi:10.1038/s41561-021-00880-4
- Sperner, B., Lorenz, F., Bonjer, K., Hettel, S., Müller, B., and Wenzel, F. (2001). Slab Break-Off - Abrupt Cut or Gradual Detachment? New Insights from the Vrancea Region (SE Carpathians, Romania). *Terra Nova* 13, 172–179. doi:10.1046/j.1365-3121.2001.00335.x
- Stern, R. J., and Gerya, T. (2018). Subduction Initiation in Nature and Models: A Review. *Tectonophysics* 746, 173–198. doi:10.1016/j.tecto.2017.10.014
- Stern, R. (2004). Subduction Initiation: Spontaneous and Induced. *Earth Planet. Sci. Lett.* 226, 275–292. doi:10.1016/s0012-821x(04)00498-4
- Takeuchi, C. S., and Fialko, Y. (2012). Dynamic Models of Interseismic Deformation and Stress Transfer from Plate Motion to continental Transform Faults. *J. Geophys. Res. Solid Earth* 117. doi:10.1029/2011jb009056
- Thielmann, M., and Kaus, B. J. P. (2012). Shear Heating Induced Lithospheric-Scale Localization: Does it Result in Subduction? *Earth Planet. Sci. Lett.* 359–360, 1–13. doi:10.1016/j.epsl.2012.10.002
- Thielmann, M., and Schmalholz, S. M. (2020). Contributions of Grain Damage, thermal Weakening, and Necking to Slab Detachment. *Front. Earth Sci.* 8, 254. doi:10.3389/feart.2020.00254
- Turcotte, D., and Schubert, G. (2014). *Geodynamics*. Cambridge: Cambridge University Press.
- van Hunen, J., and Allen, M. B. (2011). Continental Collision and Slab Break-Off: A Comparison of 3-d Numerical Models with Observations. *Earth Planet. Sci. Lett.* 302, 27–37. doi:10.1016/j.epsl.2010.11.035
- von Tscharn, M., Schmalholz, S. M., and Duretz, T. (2014). Three-dimensional Necking during Viscous Slab Detachment. *Geophys. Res. Lett.* 41, 4194–4200. doi:10.1002/2014GL060075
- Wenzel, F., Achauer, U., Enescu, D., Kissling, E., Russo, R., Mocanu, V., et al. (1998). Detailed Look at Final Stage of Plate Break-Off Is Target of Study in Romania. *Eos Trans. AGU* 79, 589–594. doi:10.1029/98e00427
- White, S. H., and Knipe, R. J. (1978). Transformation- and Reaction-Enhanced Ductility in Rocks. *J. Geol. Soc.* 135, 513–516. doi:10.1144/gsjgs.135.5.0513
- Yuen, D. A., Fleitout, L., Schubert, G., and Froidevaux, C. (1978). Shear Deformation Zones along Major Transform Faults and Subducting Slabs. *Geophys. J. Int.* 54, 93–119. doi:10.1111/j.1365-246x.1978.tb06758.x
- Zhao, L., Paul, A., Malusà, M. G., Xu, X., Zheng, T., Solarino, S., et al. (2016). Continuity of the alpine Slab Unraveled by High-Resolution P Wave Tomography. *J. Geophys. Res. Solid Earth* 121, 8720–8737. doi:10.1002/2016jb013310
- Zhong, X., and Li, Z.-H. (2020). Subduction Initiation during Collision-Induced Subduction Transference: Numerical Modeling and Implications for the Tethyan Evolution. *J. Geophys. Res. Solid Earth* 125, e2019JB019288. doi:10.1029/2019jb019288
- Zhou, X., Li, Z. H., Gerya, T. V., and Stern, R. J. (2020). Lateral Propagation-Induced Subduction Initiation at Passive continental Margins Controlled by Preexisting Lithospheric Weakness. *Sci. Adv.* 6, eaaz1048. doi:10.1126/sciadv.aaz1048
- Zhou, X., and Wada, I. (2021). Differentiating Induced versus Spontaneous Subduction Initiation Using Thermomechanical Models and Metamorphic Soles. *Nat. Commun.* 12, 1–10. doi:10.1038/s41467-021-24896-x

**Conflict of Interest:** The authors declare that the research was conducted in the absence of any commercial or financial relationships that could be construed as a potential conflict of interest.

**Publisher's Note:** All claims expressed in this article are solely those of the authors and do not necessarily represent those of their affiliated organizations, or those of the publisher, the editors and the reviewers. Any product that may be evaluated in this article, or claim that may be made by its manufacturer, is not guaranteed or endorsed by the publisher.

Copyright © 2022 Candiotti, Duretz and Schmalholz. This is an open-access article distributed under the terms of the Creative Commons Attribution License (CC BY). The use, distribution or reproduction in other forums is permitted, provided the original author(s) and the copyright owner(s) are credited and that the original publication in this journal is cited, in accordance with accepted academic practice. No use, distribution or reproduction is permitted which does not comply with these terms.